ABSTRACT

Title of thesis: GUST DISTURBANCE ANALYSIS OF A MICRO QUADROTOR HELICOPTER

Douglas Paul Szczublewski, Master of Science, 2012

Thesis directed by: Professor J. Sean Humbert
Department of Aerospace Engineering

Micro Air Vehicles (MAVs) are being developed for their envisioned applications in hostile urban environments where they can provide a tactical advantage to the war fighter. A vehicle at this scale faces many challenges; this paper aims to provide measures for one of these challenges. MAVs are small, lightweight and highly agile vehicles, but their low mass and inertia properties cause this class of vehicle to be highly susceptible to gust disturbances. This dissertation will focus on building measures to analyze a vehicle's performance when subjected to gust disturbances. The study will concentrate on a 70 gram quadrotor using the linear time invariant model extracted from system identification through flight test, as well as bench-top testing. The analyses explored here will leverage well-known linear system tools, including gramians and singular value decompositions. The techniques developed are easily extended to any platform and can provide key insight into trade studies when determining platform selection, configuration and layout. The ultimate goal is to determine the strengths and weaknesses of a vehicle amidst gust disturbances.

GUST DISTURBANCE ANALYSIS OF A MICRO QUADROTOR HELICOPTER

by

Douglas Paul Szczublewski

Thesis submitted to the Faculty of the Graduate School of the
University of Maryland, College Park in partial fulfillment
of the requirements for the degree of
Master of Science
2012

Advisory Committee:
Professor J. Sean Humbert Chair/Advisor
Professor Roberto Celi
Professor Anya R. Jones

Acknowledgments

This process has been an amazing ride, and I owe many thanks to the people who have supported me through this phase of my life. Without these people, none of this would have happened.

Dr. Humbert, thank you for providing me to the opportunity to join the Autonomous Vehicle Lab. Your support and advice have been invaluable for my growth and development at Maryland. Dr. Humbert's pitch line to me when I came and visited was, "Doug, I have the coolest lab." I can now attest this is true; not only is there amazing work being done in the AVL, but the people who make up the lab are phenomenal. I owe a lot to Nick Kostreski. Together we survived the grueling graduate classes together and provided countless hours of comedic relief to one another on a regular basis. Nick helped me keep a balanced lifestyle with rock climbing and triathlon training. Derek Miller, my favorite ginger, thank you for getting me up to speed on the microquad and sharing in the frustrations that we encountered along the way. Thank you Greg Gremillion for being the glue that holds the lab together. Thank you Renee Campbell for partaking in the late night pow-wows that enabled those big research pushes. Ken MacFarlane, I will miss our morning chats over a cup of coffee. Thanks to Badri Ranganathan, for being the programming expert in the lab. Thank you Steve Gerardi for being, well Steve Gerardi. Thanks to Joe Conroy on all your guidance and awkward dances that provided hours of entertainment.

I owe a special thanks to the Air Force Research Lab for providing me the opportunity to attend Maryland. Their commitment and support throughout my career is greatly appreciated. Without their support, I would never have had the opportunity to pursue graduate school at the University of Maryland. Specifically, I would like to thank Chris Greek, Dr. Greg Parker, Dr. Dave Domain, Dr. Michael Ol and Dr. Craig Cox for their guidance and support.

I would like to thank the faculty at the University of Maryland. Graduate school has been a challenge like no other I have ever encountered in life. I appreciate the high expectations that you set forth, that pushed me to limits I never thought possible. I feel honored to have learned from some the best minds academia has to offer.

Finally, to my family and friends, thank you for all your caring and loving support throughout my life. A special thanks to my dad, Dave Szczublewski. He has had a profound impact on my life, and I am truly grateful for having a role model, friend and dad all in the same person. Thank you to my sister, Kelly Montgomery, for keeping a steady supply of pictures of my nephew, Jackson. Also thanks for taking care of all my family obligations; next year I promise to do the Christmas shopping. I owe a thank you to my kayak family for providing an avenue of stress relief. Kayaking kept me grounded and a smile on my face. To Jeremy Knittel and Pete Robie, thank you for all the adventures we had together, they will never be forgotten. Pete Robie is an amazing person, but was in an unfortunate car accident. I pray for you buddy and hope one day you can fully recover. I miss you buddy!

Table of Contents

List of Tables

List of Figures

Nomenclature

$\mathbf{A}$	Dynamics Matrix
$\mathbf{A}_{CL}$	Closed Loop Dynamics Matrix
$\mathbf{B}$	Controls Matrix
$\mathbf{C}$	Sensor Matrix
$\mathbf{D}$	Disturbance Matrix
$\vec{d}$	Disturbance Vector
d_u, d_v, d_w	Translational Disturbances
d_p, d_q, d_r	Rotational Disturbances
F_x, F_y, F_z	Force Measurements
F_c	Centripetal Force
$G(s)$	Transfer Function Matrix for Vehicle
$G_d(s)$	Disturbance Transfer Function Matrix for Vehicle
$\mathbf{K}$	Static Gain Matrix
L, M, N	Body Moments
p, q, r	Roll, Pitch and Yaw rates
$\mathbf{Q}$	Weighted Matrix for States
$\mathbf{R}$	Weighted Matrix for Control Inputs
T_x, T_y, T_z	Torque Measurements
t	Time
$\vec{u}$	Control Signal Vector
u, v, w	Body Translational Rate
$\vec{x}$	Dynamic State Vector
X, Y, Z	Body Forces
x, y, z	Vehicle Inertial Position
X_c	Controllability (Reachability) Gramian
X_d	Disturbance Gramian
$\vec{z}$	Exogenous Inputs
$\vec{y}$	Output Vector
$\Lambda(G)$	Relative Gain Array
$\gamma(G)$	Condition Number
$\gamma_d(G)$	Disturbance Condition Number
ϕ, θ, ψ	Roll, Pitch, and Yaw Angle
$\delta_{lon}, \delta_{lat}, \delta_{yaw}, \delta_{thr}$	Control Inputs
ω	Angular Velocity
ω_B	Bandwidth
ρ	Disturbance Control Energy

	Abbreviations
AVL	Autonomous Vehicles Laboratory
CCD	Charge-Couple Device
CG	Center of Gravity
COTS	Commercial Off The Shelf
CTA	Collaborative Technology Alliance
DAQ	Data Acquisition
DOF	Degree of Freedom
ESC	Electronic Speed Controller
F/T	Force and Torque
FFT	Fast Fourier Transform
GINA	Guidance and Inertial Navigation Assistant
GPS	Global Positioning System
Hz	Hertz
ISR	Intelligence, Surveillance, and Reconnaissance
LED	Light Emitting Diode
LQG	Linear Quadratic Gaussian
LQR	Linear Quadratic Regulator
LTI	Linear Time Invariant
MAST	Micro Autonomous Systems Technology
MAV	Unmanned Air Vehicle
MIMO	Multiple Input Multiple Output
PSD	Power Density Spectrum
PWM	Pulse Width Modulation
RGA	Relative Gain Array
RPM	Revolutions Per Minute
RPS	Revolutions Per Second
SEP	Spherical Error Probability
SISO	Single Input Since Output
SVD	Singular Value Decomposition
TFM	Transfer Function Matrix

Chapter 1

Introduction

There has been recent interest in the potential tactical advantages a small, agile vehicle can provide in an urban environment. A large number of military causalities happen in a confined environment. The enemy has the advantage of knowledge of their surroundings. Intelligence, Surveillance, and Reconnaissance (ISR) capability in recent years has provided military forces information to execute aggressive and successful battle strategies against hostile targets. Due to the success of ISR capability there is an increase demand for the concept of layered sensing, which provides information to the war fighter from different vantage points. One crucial component that is missing is the ability to scout caves, buildings, and urban settings. For this flight regime, Micro Air Vehicles (MAVs) can play a crucial role in closing the gap of essential information to the war fighter.

There are several challenges to overcome in an urban environment. Autonomous flight heavily relies on Global Positioning System (GPS), which can become intermittent or non-existent due to loss of line of sight with GPS satellites. Communication between the vehicle and ground station also poses a problem for the same reason. Since vehicles are operating close to the earth, they are not able to loiter above valuable targets, thereby making hover and perching more ideal for ISR in this environment. Yet hovering is often energy intensive, and perching is a definitively complex maneuver that has yet to be perfected in areas with limited sensing. The flight space has many obstacles such as power lines, buildings and gust disturbances. Even on a calm day, wind gusts can become violent due to buildings funneling any slight breeze. This paper will focus on analysis tools to evaluate vehicles against expected disturbances and will explore the limitations of disturbance rejection.

There is limited work on disturbance rejection at this scale. A study at Georgia Institute of Technology [1] used a Walkera$^{\text{TM}}$ micro coaxial helicopter and tested its performance in an array of gust scenarios. In hover condition the Spherical Error Probability (SEP) was tracked, which only measured the variations of the vehicle from its commanded position. Trajectory tracking was also evaluated by looking at the error between the desired trajectory and the actual flight path of the coaxial helicopter. This type of testing provides little insight about how this class of vehicle operates in wind gust. Instead, it provided only the performance of a coaxial helicopter for these specific scenarios. The coaxial helicopter is known to have limited agility due to being an inherently stable platform. Similarly, University of Maryland evaluated the performance of an X-UFO Quadrotor with optic flow measurements tied into the control law [2]. This study looked at the setting time of a vehicle when faced with a steady gust disturbance from a box fan. Again this study only tested one vehicle in a specific disturbance condition and provided limited information on how MAVs perform in these types of environment.

Alternatively, Pisano took a different approach through an examination of varying flight characteristics in the frequency domain, and observed how they change when scaled by size [3]. Doing so provides basic metrics for actuator bandwidth, update rates for gyros/sensor measurements and necessary closed loop bandwidth of the vehicle. These three parameters where scaled with wingspan, which is ultimately related to the vehicle's inertia properties. Small moments of inertias result in faster natural modes, therefore requiring increased bandwidth on actuation and close loop performance. The faster dynamics also require higher bandwidth for measurements from the sensor packages. This investigation provides key insight into design requirements at this scale.

The body of work presented in this paper supports the Micro Autonomous Systems Technology (MAST) Collaborative Technology Alliance (CTA) effort. This effort focuses on an array of objectives. One of the goals is to provide models of several vehicle platforms at this scale and compare performance of the vehicles with different metrics. The metric examined in this paper is the vehicles disturbance rejection properties. Once a model has been identified, this method can be performed to examine the platforms traits against various disturbances. The MAST CTA focuses on an array of vehicles including quadrotors, single and coaxial helicopters, cyclocopters and flappers. Once models are identified for these platforms the disturbance analysis outlined here can be applied. This will highlight each platform's vulnerabilities and strengths, and provide a layer of understanding of how different platforms at this scale perform under different disturbance conditions.

The methods for examining disturbance properties will use a 70 gram quadrotor that has a span of 6 inches from rotor tip to rotor tip. This small size gives the vehicle low inertia properties resulting in fast body dynamics. This is a desirable trait since it allows the vehicle to be highly agile; it only takes a small amount of control authority to create moments and forces on the vehicle. This particular quadrotor is inherently unstable. Fighter jets also possess this trait, and this instability adds to the vehicle's agility. The rotors are arranged in an "X" configuration, which differs from the conventional plus layout. Though this approach is slightly more complex, in principle it provides more control authority owing to the fact that the rotors are involved in each maneuver. A quadrotor is ideal for developing this methodology due to its intuitive flight control layout.

The purpose of this dissertation is to investigate the disturbance properties of the microquad. The list below outlines the contributions, which when coupled together present an all-encompassing method of analysis that provides key insight into microquad sensitivity to disturbances and its ability to reject them.

- Identify disturbance matrix from the microquad through an experimental setup.
- Develop framework for gramian based analysis aimed to determine maximum disturbances the microquad is able to reject given a bounded control input. These results are subsequently verified through simulations.
- Explore the directionality of the disturbance as it relates to the plant dynamics of the microquad.
- Examine relative control energy required for each disturbance parameter.
- Investigate actuator bandwidth as it relates to the dynamics of a disturbance.

Chapter 2

Quadrotor Overview

2.1 Vehicle Configuration

Quadrotors are the vehicle of choice for many research laboratories. They make an excellent test platform due to their simplistic design and favorable thrust to weight ratio allowing the vehicle to carry large payloads in relation to their size. Typically these vehicles are used for sensor package and navigation algorithm development. The Autonomous Vehicles Laboratory (AVL) at the University of Maryland has been developing a microquad intended to push the limits of Micro Air Vehicle development and provide a better understanding of the limits of vehicles at this scale. The ultimate goal is to demonstrate that a vehicle of this size can successfully navigate in a GPS denied urban environment.

MAVs have many obstacles to overcome in their development. Their low inertias make the dynamics of the vehicle very fast, resulting in a highly agile vehicle. As a result, high bandwidth actuation is required to control the vehicles fast dynamics. Although there have been great advancements in electronics and processing, power continuous to be a limited resource at this scale. Powerful processors require large amounts of power, which in turn requires larger sources of power, typically lithium polymer batteries. Battery technology continues to be a bottleneck for long duration missions. Currently, the microquad has a flight duration of approximately ten minutes; it is doubtful that any mission could be completed in that amount of time. Another issue at this scale is its limited payload capability, making it difficult to have redundant sensors for robustness. The microquad still has many challenges before it can become a viable platform, but this iteration will provide insight on the technology gaps that lie ahead and provide a baseline as to what can be accomplished at this scale.

Quadrotors are typically arranged in a plus configuration with two sets of rotors: one set rotating counter-clockwise and the other set clockwise. This is depicted in Figure 2.1 from [15] and will be used to describe how a quadrotor maneuvers. For a flight condition of hover, all four rotors provide an identical amount of thrust equal to the weight of the vehicle. Altitude is controlled by increasing and decreasing all four rotors in unison. The two sets of contour rotating rotors provide the torque required to maintain a heading lock. Having a differential in RPM between the two sets of rotors causes a yaw moment. For example, having rotors one and three decrease RPM, and rotors two and four increase RPM to compensate for the loss in thrust will result in a counter-clockwise rotation of the vehicle. In order to move forward and aft, pitching the vehicle is required and is achieved by a difference in thrust from opposing rotors. The same is true for lateral motions. These basics movements are fairly decoupled and will be broken down into heaver, yaw, longitudinal and lateral dynamics depicted in [5].

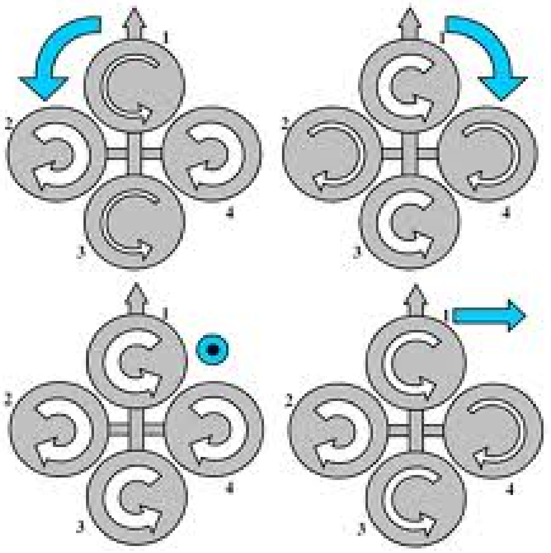

Figure 2.1: Mechanics of a Cross Configuration Quadrotor

For the microquad an “X” configuration was settled on for the design. The reasoning is that this layout requires more actuators to be involved for each maneuver. The benefit is additional control authority; however, the downside is added complexity when mixing the control inputs to motor actuation. The basic control concept is the same as the plus configuration, but rotated 90 degrees, requiring all four motors for longitudinal and lateral movements. Figure 2.2 depicts how more rotors are involved in longitudinal, lateral and yaw maneuvers. For instance, to translate right, the vehicle needs to roll right. The desired attitude is achieved by decreasing RPM on the right two rotors and increasing RPM the left rotors resulting in the microquad to transverse to the right.

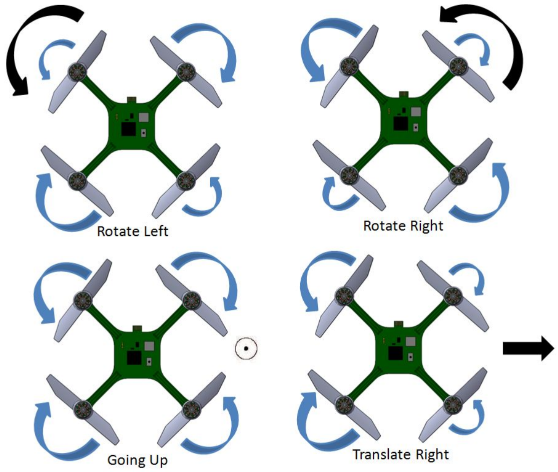

Figure 2.2: Mechanics of a “X” Configuration Quadrotor

The microquad is inherently unstable and requires rate gyros coupled inner-loop feedback to maintain the attitude of the vehicle. This instability makes the vehicle highly maneuverable, but also requires adequate sensing and control bandwidth to leverage these desired flight characteristics. To control these fast inner-loop dynamics, the Guidance and Inertial Navigation Assistant (GINA) mote, developed at the University of California Berkeley, is utilized for the avionics package. The current microquad has the GINA 2.2c mote installed, which boasts Kionix$^{\text{TM}}$ KXSD9-1026 accelerometer and the InvenSense$^{\text{TM}}$ ITG3200 gyroscope. The rate gyroscope aids in damping for the inner-loop of the vehicle allowing it to be stabilized. Damping adds stiffness to the system and slows down the dynamics. A complimentary filter blends the measures from the accelerometer and gyroscopes together to provide an estimate for the pitch θ and roll ϕ angles [15]. Having an accurate estimate of the vehicle’s attitude is imperative for controlling the microquad in longitudinal and lateral directions.

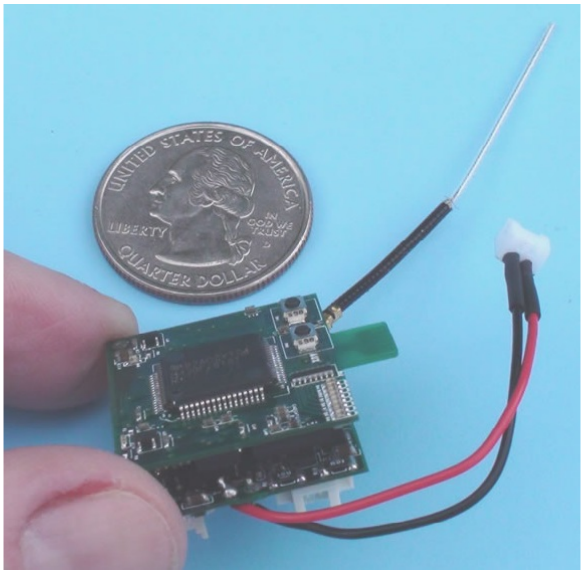

Figure 2.3: University of California Berkeley GINA Mote

The GINA mote handles sensing, processing, and communication for the vehicles. The GINA mote seen in Figure 2.3 is equipped with a Texas Instruments MSP430 microcontroller that operates at a 333 Hz loop time. This can be varied depending on application. The lightweight sensor suite weighs 2 grams and carries a 3-axis rate gyroscope and two 3-axis accelerometers. The board has a 2.4 GHz Atmel AT86RF230 radio which is capable of bi-directional communication; therefore, information is able to be transmitted and received. Communication to the ground station is carried out by a USB Atmel RZ600 base station mote. The communication architecture is depicted in Figure 2.4. The on-board microcontroller handles all data processing and communications, as well as generating PWM signals to the microquad's Electronic Speed Controllers (ESCs). The ESCs ultimately drive the four rotors. The GINA mote requires 3.7 volt power source, which is the typical output voltage of a single cell battery. This lower power, light weight sensor suite is an effective avionics package at this scale.

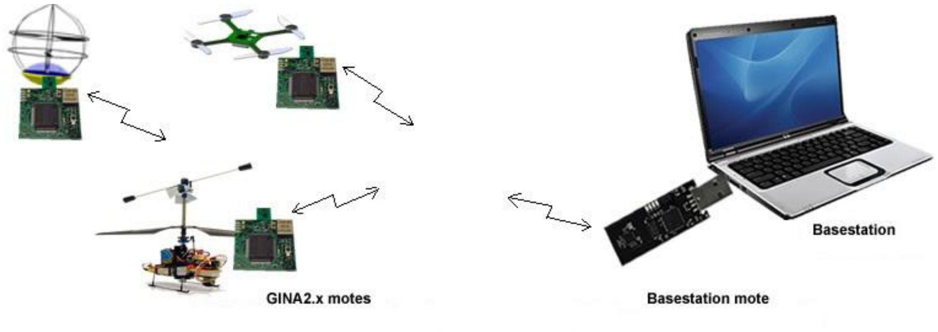

Figure 2.4: Communication Architecture

The microquad is equipped with 4 Walkera^{TM} ESCs that drive 4 KV7500 brushless motors with 4 GWS^{TM} counter-rotating 3x2 propellers. All these components were designed to operate with a 3.7 volt power source. The vehicle's power supply is a 2 cell lithium polymer battery, which is rated for 7.4 volts. A power regulator break-out board, Figure 2.5, was designed to step down the 7.4 volts to 3.7 volts. This is the operating voltage for all of the electrical components installed on the microquad. This solution was implemented to gain more consistent performance throughout the duration of a flight. Using a power regular mitigates the problem of battery degradation over a course of a flight. For example, a single cell LiPo provides 4.3 volts when fully changed and will nonlinearly degrade to 3.5 volts. During this degradation of power, the vehicle performs vastly different, making tuning gains extremely difficult because consistent performance cannot be attained.

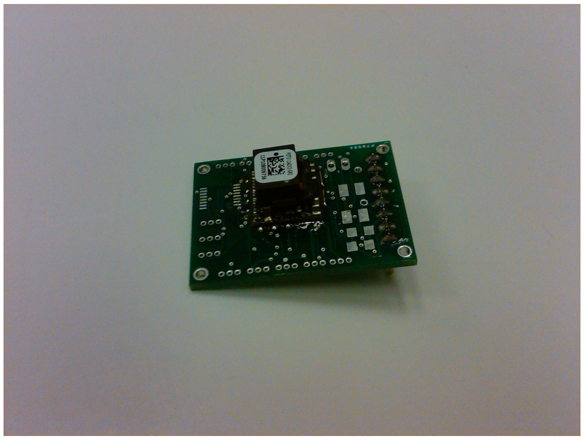

Figure 2.5: Power Regulation Breakout Board

This is the fifth generation microquad and is shown in Figure 2.6. Each new iteration dealt with issues that the previous design encountered; these issues are discussed in detail by Miller [15]. The current microquad has demonstrated reliable open-loop flights with damping feedback, provided by the rate gyroscopes. Using damping feedback allows a pilot to fly the vehicle open-loop. With this ability, system identification has been performed and a Linear Time Invariant (LTI) model has been constructed by Miller [15]. Additionally, model based controllers have been developed to control the outer-loop for position hold. These model based controllers have not been successfully implemented as planned, due to actuation issues from the Commercial Off The Shelf (COTS) ESCs. These ESCs are low quality and do not have the desired precision and accuracy required to maintain position hold. Currently, this issue is being addressed by designing an in-house ESC. Although the vehicle will not be flight tested for its disturbance properties, information about the vehicle disturbance resiliency can be explored through the methodology presented here.

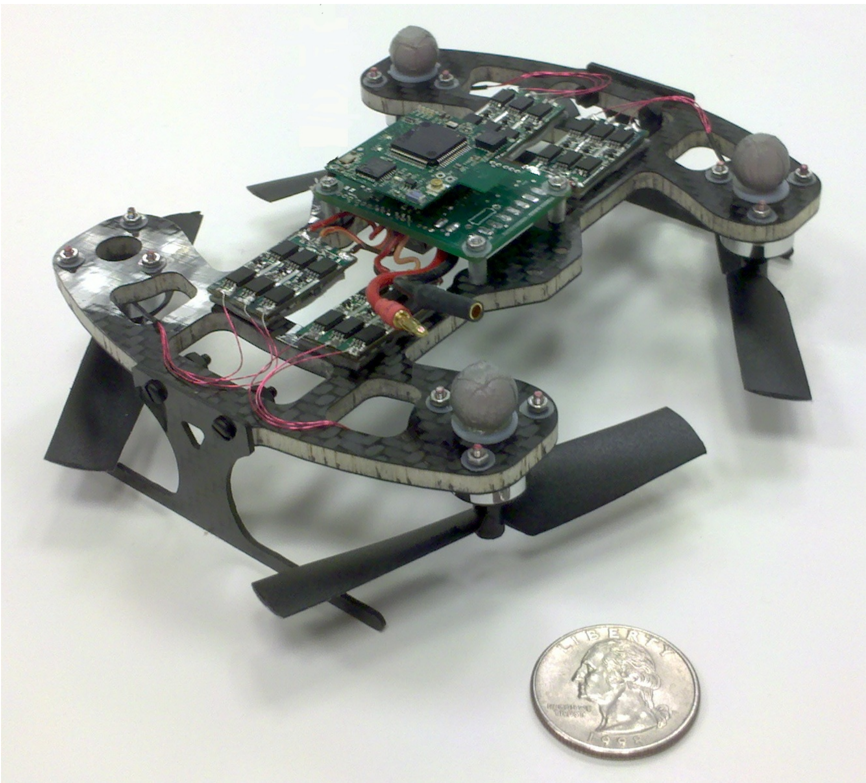

Figure 2.6: Microquad Version 5

Chapter 3

Vehicle Model

3.1 Overview

Having an accurate system model for a vehicle is vital for evaluating vehicle performance, flight characteristics and controller development. The common state space representation is a useful formulation that is supported by well-developed theory and powerful tools for both analysis and controller design. Equation 3.1 is the typical state space model realization, which is presented in any multi-variable linear controls book [13], [20]. In this formulation $\vec{x}$ is the state vector, $\dot{\vec{x}}$ is the time derivative of the state vector, $\vec{u}$ is the control input vector, and $\vec{y}$ is the measurements vector. Matrix **A** describes the system's dynamics, **B** is the control matrix, **C** is the observation matrix, and **D** is the feedforward matrix. Matrix **D** will always be zero and will be eliminated from the model.

$$\begin{aligned} \dot{\vec{x}} &= \mathbf{A}\vec{x} + \mathbf{B}\vec{u} \\ \vec{y} &= \mathbf{C}\vec{x} + \mathbf{D}\vec{u} \end{aligned} \tag{3.1}$$

Linear time invariant models relate the inputs and outputs of the system, which is typically represented in a block diagram format as seen in Figure 3.1, where **G** is the system dynamics from the state space model and sometimes is referred to as the plant. Block diagram models are a useful tool when visualizing the structure of a system and can also aid in control design synthesis.

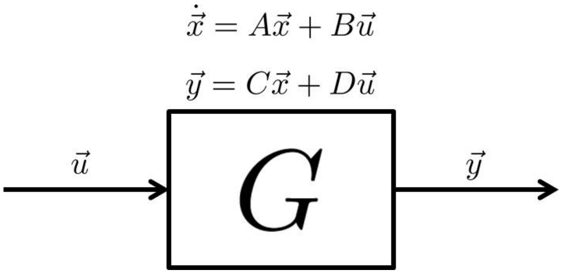

Figure 3.1: Block Diagram of the System Dynamics

An additional **D** matrix is added to the state equation to account for disturbances. This disturbance matrix is different from the **D** feedforward matrix and should not be confused. As stated previously, the feedforward matrix will be zero; therefore from here on, **D** will denote the disturbance matrix. The **D** matrix can be thought of as a controls matrix with $\vec{d}$ as the input. In reality, the disturbances are not an input that is controlled, but thinking of it in this context will aid in the analysis process, which will be seen in subsequent chapters. Since superposition is a linear property, the contribution from the control input and distance input can simply be added together.

$$\begin{aligned} \dot{\vec{x}} &= \mathbf{A}\vec{x} + \mathbf{B}\vec{u} + \mathbf{D}\vec{d} \\ \vec{y} &= \mathbf{C}\vec{x} \end{aligned} \tag{3.2}$$

3.2 System Identification

This chapter builds on the previous work of Miller [15] and will provide a brief overview of the system identification techniques used to extract a bare air frame model of the microquad. The control inputs and outputs of the system are recorded, and then the data is post-processed using linear regression techniques to determine stability and control derivatives, which are contained in the state space model. Once a model is extracted, it is verified by using other sets of flight data as truth data, and finally the truth data can be compared with what the final model predicts.

The standard state space structure, $\dot{\vec{x}} = A\vec{x} + B\vec{u}$, was employed for the system model. A first principle model approach is used to identify the dominant terms. This model closely emulates the results from Gremillion [5]. The results of the linearization is seen in Equation 3.3 and shows the dominate stability and control derivatives. This is essential when performing system identification with SIDPAC [16], a software package developed in Matlab$^{\text{TM}}$, to aid in the system identification process using flight data. This software package has tools for both time domain and frequency domain methods. For the identified model for the microquad, a linear regression algorithm determined the coefficients to fit the time domain flight data. These coefficients are referred to as stability derivatives.

Equation 3.3, from Miller [15], shows the LTI model, where the state vector is $\vec{x} = [u, v, w, p, q, r, \phi, \theta, \psi]^T$ and the control inputs are $\vec{u} = [\delta_{lon}, \delta_{lat}, \delta_{yaw}, \delta_{thr}]^T$. This model represents the bare air frame inner-loop vehicle dynamics. The terms that populate the dynamics matrix **A** are referred to as stability derivatives. The terms in the controls matrix **B** are control derivatives. These are partial derivatives for the forces and moments acting on the vehicle and the subscript indicates the cause of the resulting force or moment. Forces are denoted as $[X, Y, Z]^T$, where X is a force that acts in the x-body direction and so on. In a similar fashion, moments are represented by $[L, M, N]^T$, where L is a moment about the x-body axis and so on. For example X_u is the stability derivative relating X-force cause by the forward velocity u. Stability derivatives are typically normalized by a mass term; derivatives relating force to a perturbation are normalized by mass, and stability derivatives relating moment to a perturbation are normalized by the mass moment of inertia. An example is $X_u = \frac{1}{m}\frac{\partial X}{\partial u}$. This is the same convention used in Nelson [12].

$$\dot{\vec{x}} = \begin{bmatrix} X_u & 0 & 0 & 0 & X_q & 0 & 0 & -g & 0 \\ 0 & Y_v & 0 & Y_p & 0 & 0 & g & 0 & 0 \\ 0 & 0 & Z_w & 0 & 0 & 0 & 0 & 0 & 0 \\ 0 & L_v & 0 & L_p & 0 & 0 & L_\phi & 0 & 0 \\ M_u & 0 & 0 & 0 & M_q & 0 & 0 & M_\theta & 0 \\ 0 & 0 & 0 & 0 & 0 & N_r & 0 & 0 & 0 \\ 0 & 0 & 0 & 1 & 0 & 0 & 0 & 0 & 0 \\ 0 & 0 & 0 & 0 & 1 & 0 & 0 & 0 & 0 \\ 0 & 0 & 0 & 0 & 0 & 1 & 0 & 0 & 0 \end{bmatrix} \vec{x} + \begin{bmatrix} 0 & 0 & 0 & 0 \\ 0 & 0 & 0 & 0 \\ 0 & 0 & 0 & Z_{thr} \\ 0 & L_{lat} & 0 & 0 \\ M_{lon} & 0 & 0 & 0 \\ 0 & 0 & N_{yaw} & 0 \\ 0 & 0 & 0 & 0 \\ 0 & 0 & 0 & 0 \\ 0 & 0 & 0 & 0 \end{bmatrix} \vec{u} \tag{3.3}$$

For the system identification process, it is desirable to extract a dynamics model of the system independent of control, this referred to as a bare airframe model. The microquad's inherent instability required inner-loop feedback control for it to be pilotable, making this an obstacle for extracting a bare airframe model. To identify a model with feedback control already implemented is rather pointless, as any closed-loop control effects the natural dynamics of the vehicle. This would yield an inaccurate model making controller designs suboptimal and possibly unusable. This is why extracting the bare airframe (no feedback control) is vital. This is achieved by setting feedback gains as low as possible and having knowledge of the exact control strategy. This allows the full control signal to be reconstructed by adding the pilot commands and the feedback control input together, and provides the total control input to the vehicle. Using this information coupled with state information provided by a motion capture system, allows a model to be extracted to fit the flight data.

Table 3.1 shows the longitudinal stability derivatives calculated over 10 different flights from Miller [15]. The percent error indicates how well the identified model fits the flight test data. Clearly, there is a large variation in the parameters. This is due to the stability derivatives being reliant on one another. For instance, for forward flight to occur, the vehicle needs to provide a moment that pitches the vehicle forward, tilting the thrust vector, and providing a resulting force in the x-direction, and subsequently a forward velocity. Due to this build-up effect, the weighting of X_u, X_q, M_u, and M_q can have various distributions and still adequately fit the flight data. This does not mean that the model derived does not accurately represent the system, as a system can have multiple realizations and still yield the same results. A perfect example of this is representing a system in observer canonical form and controller canonical form. Both actually represent the system, but are different realizations of the model [13]. However, in these instances, the parameters within the model lose their physical meaning, which is important when constructing the disturbance matrix $\mathbf{D}$.

X_u		X_q		M_u		M_q	
Parameter	% Error	Parameter	% Error	Parameter	% Error	Parameter	% Error
-0.2004	13.28	-0.21191	19.96	6.3642	2.38	-6.404	2.43
-0.42149	7.45	-0.06105	68.31	24.139	7.68	-25.535	7.71
-0.27055	12.22	- 0.13251	28.21	17.351	4.44	-17.098	4.45
-0.47435	5.88	0.11572	32.56	19.656	4.09	-18.835	4.15
-0.64059	7.64	0.15584	34.37	19.182	10.19	-25.257	10.00
-0.5735	7.36	0.2164	25.46	13.327	0.53	-14.377	0.51
-0.57697	6.09	0.12209	29.13	18.737	0.25	-18.67	0.21
-0.34154	8.68	-0.05345	60.65	26.415	3.72	-27.169	3.64
-0.61581	5.51	0.17822	21.06	16.716	2.87	-15.037	2.70
-0.3762	8.00	-0.07195	35.05	26.691	3.66	-23.312	3.55

Table 3.1: LTI Longitudinal Stability Derivatives

3.3 Disturbance Matrix

3.3.1 Introduction

This section focuses on identifying the disturbance parameters in the disturbance matrix. There are 3 translational and 3 rotational gust components denoted by $\vec{d} = [d_u, d_v, d_w, d_p, d_q, d_r]^T$. With an accurate model, the conventional way to model atmospheric disturbance is to select the stability derivatives for forces and moments that are influenced by $[u, v, w, p, q, r]^T$ components and negate the terms [12]. These terms are represented by $\mathbf{D} = -\mathbf{A}$ and is reflected in Equation 3.4. Similar to Equation 3.3, a number of these terms will be zero. This, however, is not done here, due to the large variations in the stability derivatives from the system identification process, which was discussed in § 3.1. Therefore, a series of bench-top tests were performed, and from this data stability derivatives were extracted.

$$\mathbf{D} = \begin{bmatrix} -X_u & -X_v & -X_w & -X_p & -X_q & -X_r \\ -Y_u & -Y_v & -Y_w & -Y_p & -Y_q & -Y_r \\ -Z_u & -Z_v & -Z_w & -Z_p & -Z_q & -Z_r \\ -L_u & -L_v & -L_w & -L_p & -L_q & -L_r \\ -M_u & -M_v & -M_w & -M_p & -M_q & -M_r \\ -N_u & -N_v & -N_w & -N_p & -N_q & -N_r \end{bmatrix} \tag{3.4}$$

3.3.2 Experimental Setup for Translational Stability Derivatives

This section will focus on the stability derivatives influenced by $[d_u, d_v, d_w]^T$ wind component, accomplished by using a fan bank to gust the microquad in a hover flight condition. The vehicle itself is rigidly mounted to a 6 Degree of Freedom (DOF) force and moment transducer. This measures the changes of the loading on the vehicle due to a particular translational disturbance, which is approximated by a linear relationship between the loading on the vehicle and the magnitude of the disturbance. The slope of this curve yields the stability derivative when normalized by its respected mass or moment of inertia, depending on whether it's a force and moment derivative.

The gust generator developed here is a simple and inexpensive test setup that is built from a array of computer fans similar to Harland [14]. A bank of fans is a versatile solution and can serve two purposes: first being a pseudo wind tunnel for bench-top experiments used to get stability derivative, and second is its envisioned use as a disturbance generator for flight test. The gust generator has the ability to pulse individual fans to simulate spatial and temporal variations. This more accurately represents what a vehicle will encounter in an urban environment. The fan bank is constructed from a matrix of 3.5 inch Superflo$^{\mathrm{TM}}$ fans, which is driven by a modified 12 volt, 250 Watt computer power supply. These DC brushless fans are controlled by a PIC18F8722 microcontroller$^{\mathrm{TM}}$ that produces PWM signal to command a duty cycle that controls the RPM of the fans. The PIC receives commands via a RS-232 cable from Labview software.

This fan bank solution is crude, but was effective and delivered the required results. A quick survey was conducted to determine the optimal location to place the microquad for testing. The fan bank has a 10.5 inch by 10.5 inch cross section, leaving little room for vehicle placement. Figure 3.2 shows the propagation of the air velocity downstream of the honey comb outlet. The red box indicates where the microquad is placed for experiments, roughly 17 inches downstream of the honey comb. The error bars are the standard deviation over recording 20 seconds of measurements which is $\sigma = 0.18 m/s$ in the area where the vehicle is placed. The span-wise velocity profile was surveyed and is indicated in Figure 3.3. Again, the red box indicates where the microquad was placed for testing. It should be noted, this setup is adequate, but not ideal. Expanding the fan bank would provide a larger test area to place the vehicle.

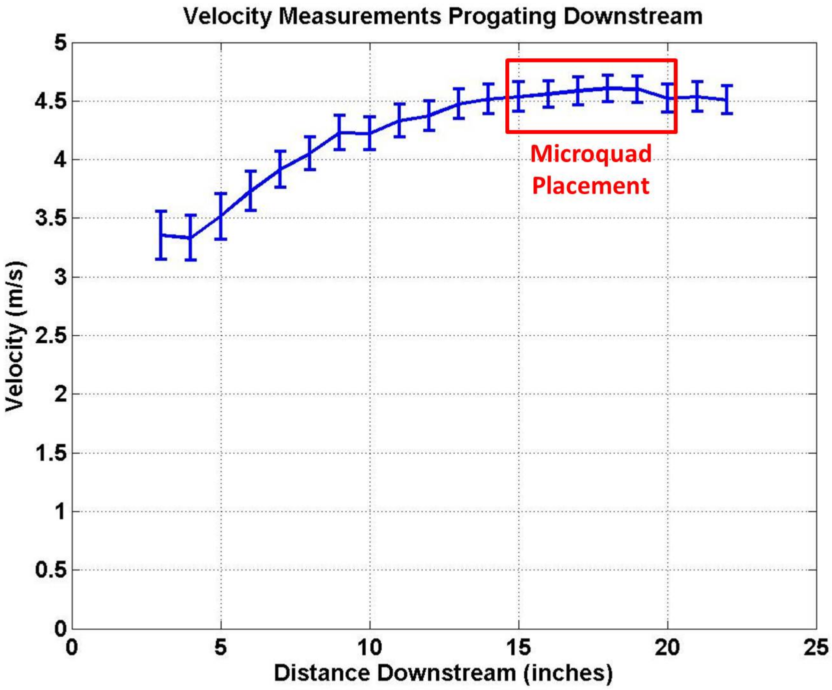

Figure 3.2: Velocity Propagation Downstream from Gust Generator

Labview^{TM} was the central hub of each experimental setup; it integrates all hardware and records all necessary data including velocity transducer measurements, force and moments transducer readings, and the RPM sensor. Labveiw^{TM} sends commands to the baystation which relays them to the GINA mote to drive the microquad's motors, as well as sending commands to the PIC microcontroller that controls the fan bank. A National Instruments^{TM} terminal block records

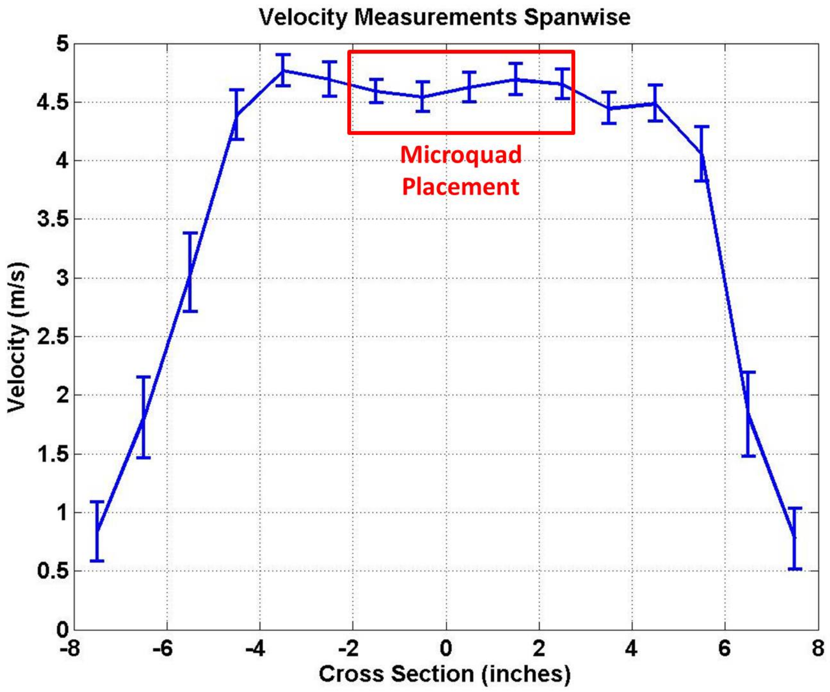

Figure 3.3: Spanwise Velocity Survey

measurements from the velocity transducer, force and moments transducer, and RPM sensor.

The microquad is mounted a Six-Axis Forces/Torques sensor system, the Nano17 Titanium Transducer, produced by ATI Industrial Automation. This is a versatile sensor that is ideal for measuring loads on the scale for MAVs. This transducer has ATI's SI-12-0.12 calibration with a max load capability of $F_x, F_y = 12N, F_z = 17N, T_x, T_y = 12N - mm$, and $T_x, T_y, T_z = 120N - mm$ with a resolution of $F_x, F_y, F_z = 1/320N$ and $T_x, T_y, T_z = 1/64N - mm$. Figure 3.4 shows how the vehicle is mounted to the F/T sensor system. Coordinate frame, $[\hat{x}_s, \hat{y}_s, \hat{z}_s]^T$, denotes the sensor measurement frame and $[\hat{x}_b, \hat{y}_b, \hat{z}_b]^T$ defines the body frame of the vehicle. It should be noted that each experiment setup had to account for a coordinate rotation and the offset distance between the sensor and the microquad. In this static case, the added moment had to be subtracted. This was easily accomplished by subtracting the force multiplied by the moment arm.

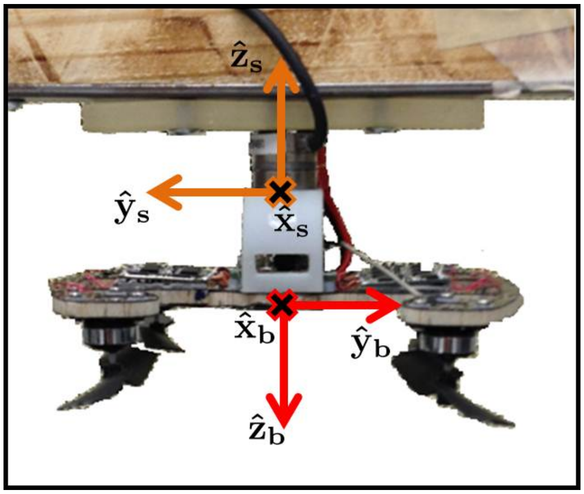

Figure 3.4: General Experimental Setup Between F/T Sensor and Microquad

Figure 3.5 depicts the setup for the vehicle encountering a u velocity disturbance. The test procedure is to send a command that puts the vehicle in a hover condition, then step through a test matrix of duty cycles for the fan bank, which changes the wind velocity. For each data point, velocity and F/T measurements were acquired for 5 seconds sampling at 7 kHz, which is the upper limit recommended for sampling with the F/T sensor. The high sample rate was needed to record RPM sensor information; however this piece of information was never needed to compute the stability derivatives.

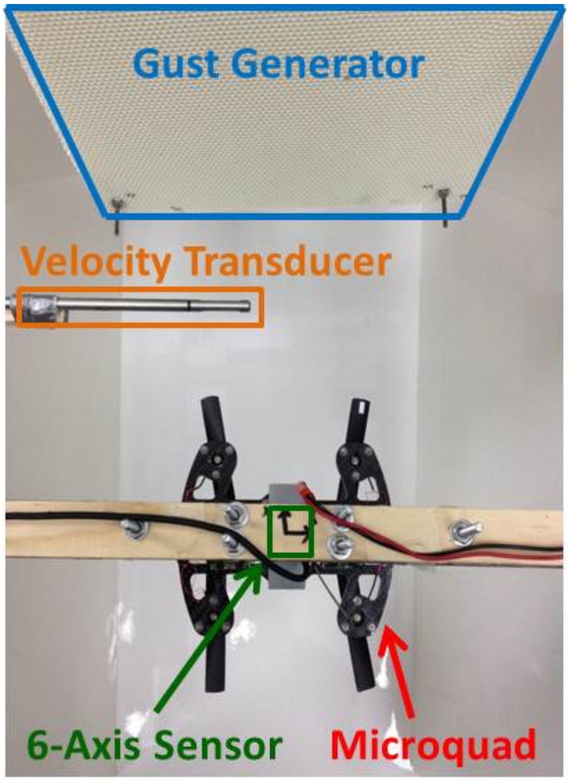

Figure 3.5: Experimental Setup for a Translational Disturbance

For v velocity disturbance, a similar configuration was employed with the vehicle rotated 90 degrees about the z-body axis. This rotation was accounted for during the data reduction process. For w velocity component, the fan bank was oriented blowing upwards with the vehicle mounted above it in an inverted fashion. This simulated a disturbance in the same direction as the z-body axis. In this configuration the microquad was positioned where the downwash from the vehicle and the air velocity are in the same direction. It should be noted that tests were performed with the downwash and wind velocity opposed to one another. The results were extremely inconstant as the air velocity and force measurements needed to be recorded in separate runs. Also the downwash from the microquad blowing into the honey comb of the gust generator caused inconsistent results.

3.3.3 Filtering Data

An obstacle encountered when processing data was large amplitude vibrations. This is common with imbalanced rotors operating at high RPM, but the magnitude of these vibrations caused concern about the accuracy of the measurement and a possible flaw in the experimental setup. Examining the radial forces in Figure 3.6 from a single motor/rotor setup caused doubt in the accuracy of the F/T sensor, as the radial forces from vibrational loading are on the same order of magnitude as the thrust produced by the rotor itself. This section examines this issue, and will determine whether this vibration noise is present as a result of imbalanced rotors. Figure 3.7 shows the frequency content of F_x component of the radial forces, which clearly shows an oscillatory loading, which one would suspect from a rotor, but the real concern is the amplitude of 0.3665 Newtons. Performing a Fast Fourier Transform (FFT) on the data, provides information as to which frequencies contribute most to the signal. As seen in Figure 3.7, the signals content is concentrated at lower frequencies with a spike at 165 Hz. This corresponds to the hover revolutions per second, which was determined to be 165 RPS from an optic sensor. This further points to a rotor imbalance that causes relatively large amplitude vibration loading.

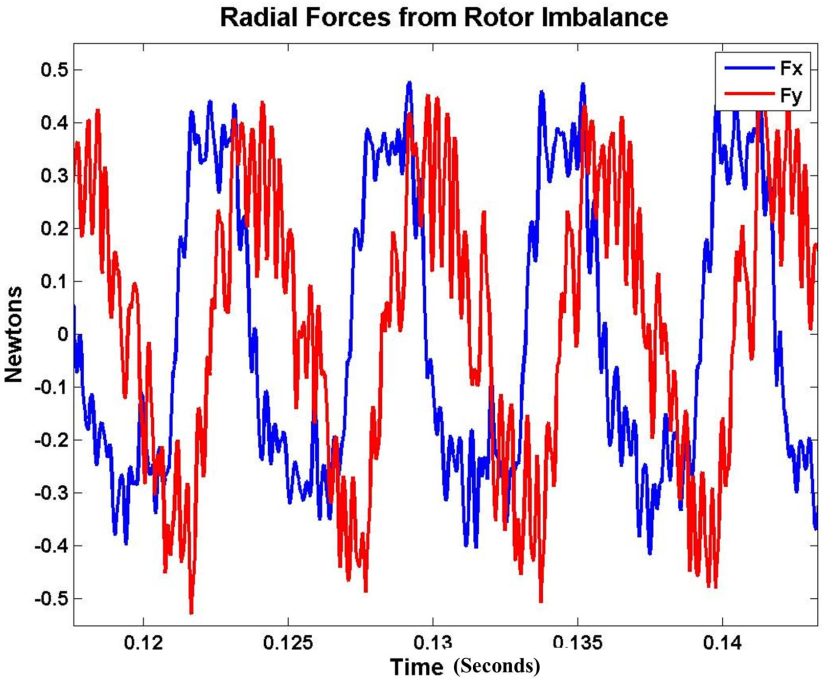

Figure 3.6: Vibrational Forces from Imbalanced Rotor

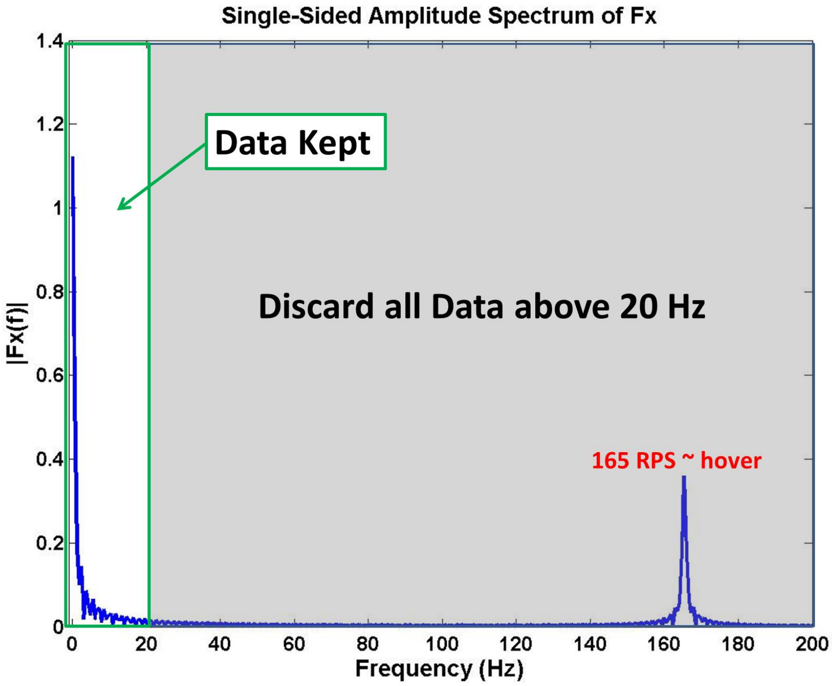

Figure 3.7: Fast Fourier Transform

An ongoing issue with the microquad development is noisy sensor data. The selection for counter-rotating rotors is quite limited at this size. The selected GWS$^{\mathrm{TM}}$ 3x2 rotors are poor quality and it is evident when comparing the consistency of each rotor. Each rotor needs to be rebalanced before being installed. This is extremely time consuming, but has shown better performance from the sensors with the procedure out lined in [15]. Although great lengths are taken to balances the rotors evenly, Figure 3.8 shows that a small mass percent imbalance in the rotors can cause large amplitude vibrations at this operational RPM. Equation 3.5 calculates the magnitude of centripetal force caused by mass imbalances, where F_c is the centripetal force, m is mass of the rotor, m_p is the mass percent of imbalance, and ω is the angular velocity. By calculating the resulting magnitude from the F_x and F_y forces and using the known RPM, the mass percent imbalance is determined to be m_p=0.1992%, which is indicated by a red ‘x’ in Figure 3.8. It is highly probable that even after balancing; the rotors can still be 0.2 % imbalanced and could easily be attributed to friction in the rotor balancing stand.

$$F_c = m m_p \omega^2 \frac{r}{2} \tag{3.5}$$

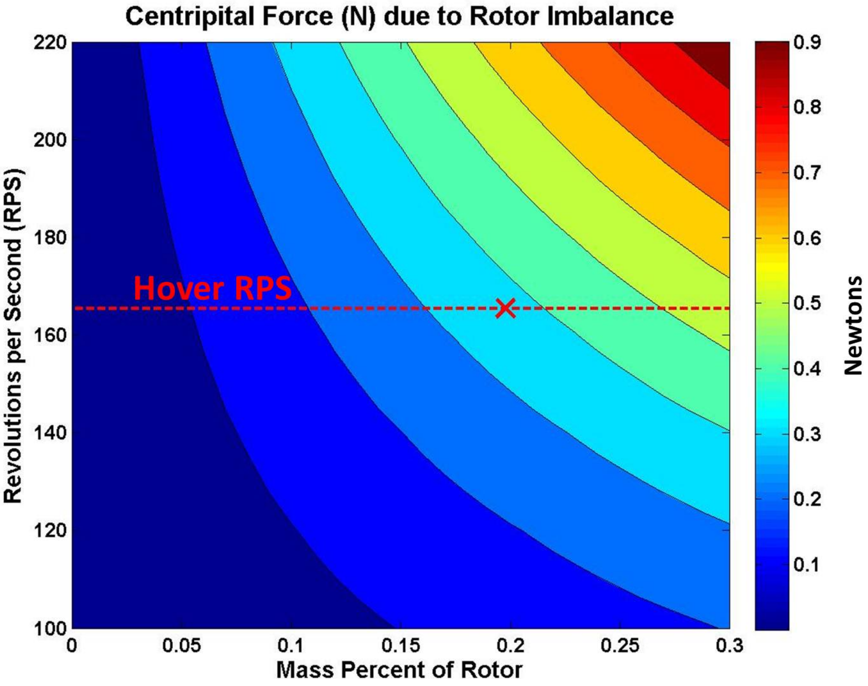

Figure 3.8: Rotor Imbalance Analysis

The results in Figure 3.6 show that there is considerable vibrational noise, which is attributed to the rotors being imbalanced, as the Figures 3.7 and 3.8 suggests. This explains the large magnitude oscillations seen in Figure 3.6. From flight data seen in Miller [15], the vehicle dynamics are well below 10 Hz. This is an order of magnitude less than the vibration loads; therefore, it can be assumed that vibrations does not affect the vehicle dynamics. Considering such, it is reasonable to filter out these vibrational loads. A fourth order Butterworth low pass filter was employed using a conservative cut-off frequency of 20 Hz. The filter design was generated from Matlab$^{\mathrm{TM}}$ using the 'butter' functions from the Filter Design Toolbox. This filtering technique will be used for all data reduction for the remainder of the test data reduction.

3.3.4 Results for Translational Stability Derivatives

Having laid to rest concerns over data, the translation components can be explored. Figure 3.9 shows how the loading on the microquad due to changes in the u velocity component. The results illustrate a strong relationship between the force in the x-direction due to the change in velocity. The error bars represent the standard deviation for each data point. F_y, F_z, T_x, and T_z have little to no slope and have a fairly large scatter. T_y has an interesting trend, which initially has a positive slope and then changes to a negative slope. This trend was repeatable over the course of 30 data points. This unexpected trend can be explained by two flaws observed in the experiment. The positive slope may be attributed to the vehicle being rigidly mounted. When throttling up to hover condition, the vehicle would flex upward due to the thrust produced by the motors. This accentually causes an increase in angle of attack, by slightly pitching up the forward two rotors into the free stream. The second observed flaw is caused by the damping material that was installed to the test apparatus to reduce vibration noise. The x-force caused by the u velocity created a moment. This became strong enough to then cause the vehicle to pitch down. These two phenomena explain the slope change for the T_y moment. As discussed earlier, this added moment was subtracted off using $F_x l$ where l is the distance between the Center of Gravity (CG) of the vehicle and sensor measuring coordinate frame. Doing so more accurately represents the loads experienced at the CG of the airframe.

Table 3.2 shows the stability derivatives, as well as the percent linear fit error. Stability derivatives are determined by dividing the slope of the linear fit curve by its respected mass property. For force terms, they are normalized by the mass of the vehicle, for example, $X_u = \frac{1}{m}\frac{\partial X}{\partial u}$. For moment terms, the slope is normalized by its respected inertia, therefore $L_u = \frac{1}{I_{xx}}\frac{\partial L}{\partial u}$. The slopes are found by using a first order 'polyfit' command in Matlab$^{\text{TM}}$. Next, the linear error fit is calculated by subtracting the measurements from the estimate provided from the linear fit curve: $e_i = z_i - y_i$ for $i = 1, 2, ..., n$, where z is the measurement, y is the estimate from the linear fit curve, and n is the number of measurements [16]. This gives a vector of error values $\vec{e}$. Taking the sum of the squares as seen in Equation 3.6, gives the fit error. This value has little significance as the magnitude needs to be scaled to put it in perspective. Therefore, a percent fit error was calculated 3.7 by taking the absolute value of the difference between the maximum measurement and the minimum measurement. This calculation measures how well the linear fit approximation fits the data set. A large error indicates a large spread in the data compared to the linear fit, which means there is weak trend and that stability derivative can be ignored. Using this logic, the only parameter of importance from the u velocity is X_u.

$$s^2 = \frac{\vec{e}^T \vec{e}}{n} \tag{3.6}$$

$$percentfiterror = \frac{\sqrt{s^2}}{||maxz - minz||} \tag{3.7}$$

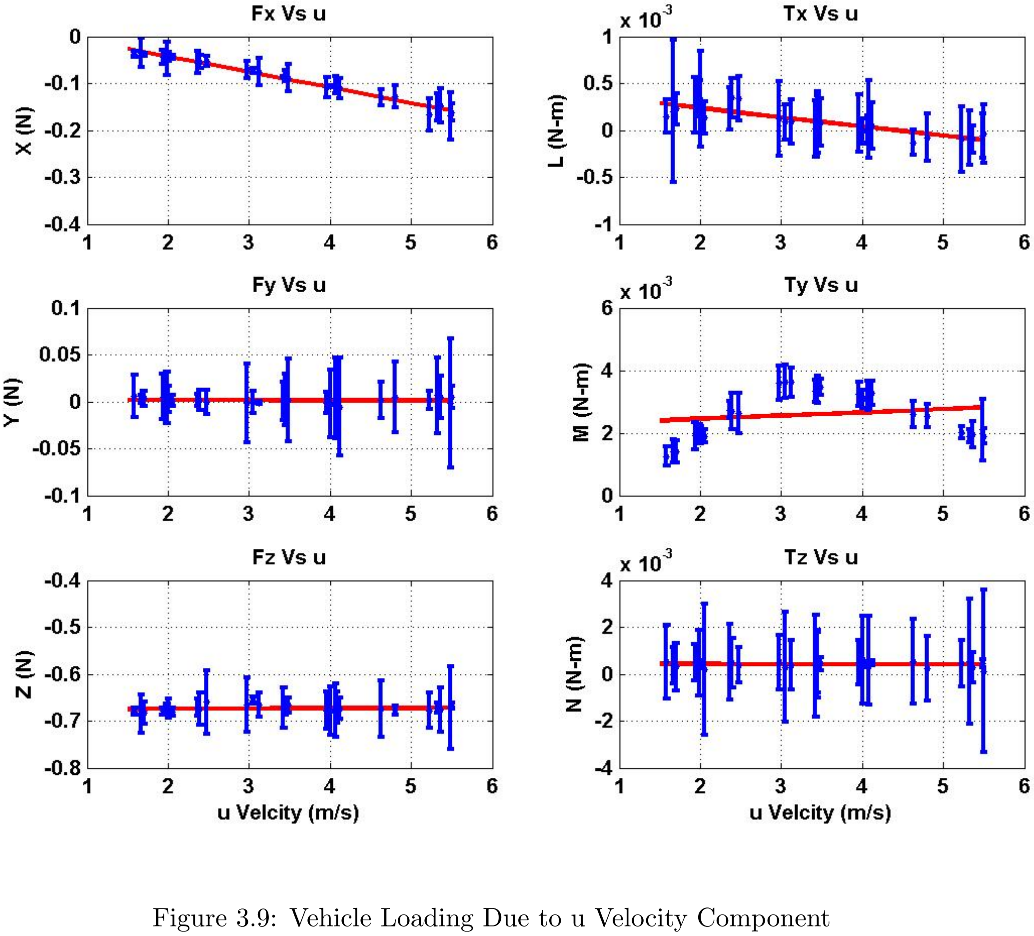

Figure 3.9: Vehicle Loading Due to u Velocity Component

Stability Derivative	Parameter	% Error Fit
X_u	-0.4703	4.3887
Y_u	-0.0019	23.1775
Z_u	0.0088	22.2764
L_u	-1.6188	14.6419
M_u	1.6962	30.6347
N_u	-0.0395	23.5370

Table 3.2: u Stability Derivatives

The results from v velocity are seen in Figure 3.10 and 3.3. This yields a similar result to the u velocity component, which is to be excepted as the vehicle is fairly symmetric about the $\hat{x_b}$ and $\hat{y_b}$ body axes. There is a weak relationship for F_x, F_z, T_x, T_y and T_z, as indicated by the percent error fit. The same trend occurs in T_x that was cause by the flexing of the vehicle and the twisting from the damping material installed in the test apparatus. There is a strong correlation between the y-force and the v velocity as expected. The only stability derivative of importance from this data set is Y_v.

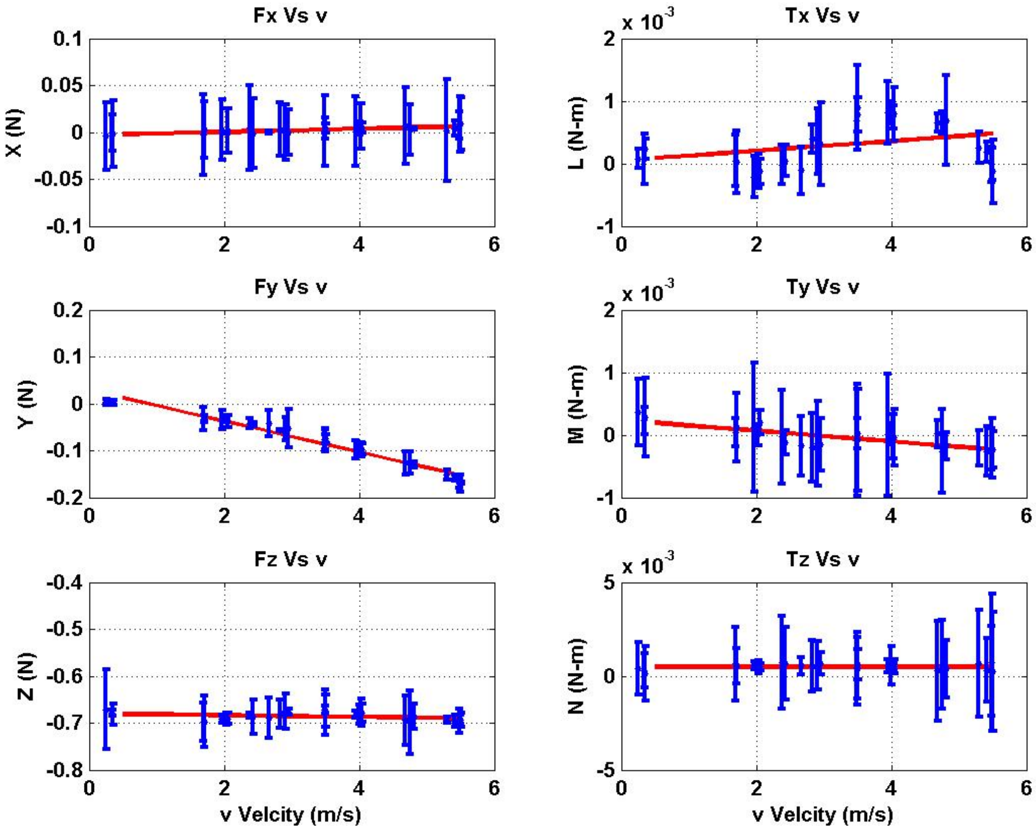

Figure 3.10: Vehicle Loading Due to v Velocity Component

Stability Derivative	Parameter	% Error Fit
X_v	0.0233	15.8952
Y_v	-0.4712	6.0404
Z_v	-0.0259	27.7602
L_v	1.2835	30.4374
M_v	-1.4077	15.6470
N_v	0.0273	26.0793

Table 3.3: v Stability Derivatives

Finally, the w velocity is considered. Recall that in this instance, the test was setup in such a way that the wind generator was blowing in the direction of the z_b body axis, hence why the w velocity is increasing negatively. Similar to the previous two tests, the only significant component is F_z for the w wind component, which is illustrated in Figure 3.11 and Table 3.4.

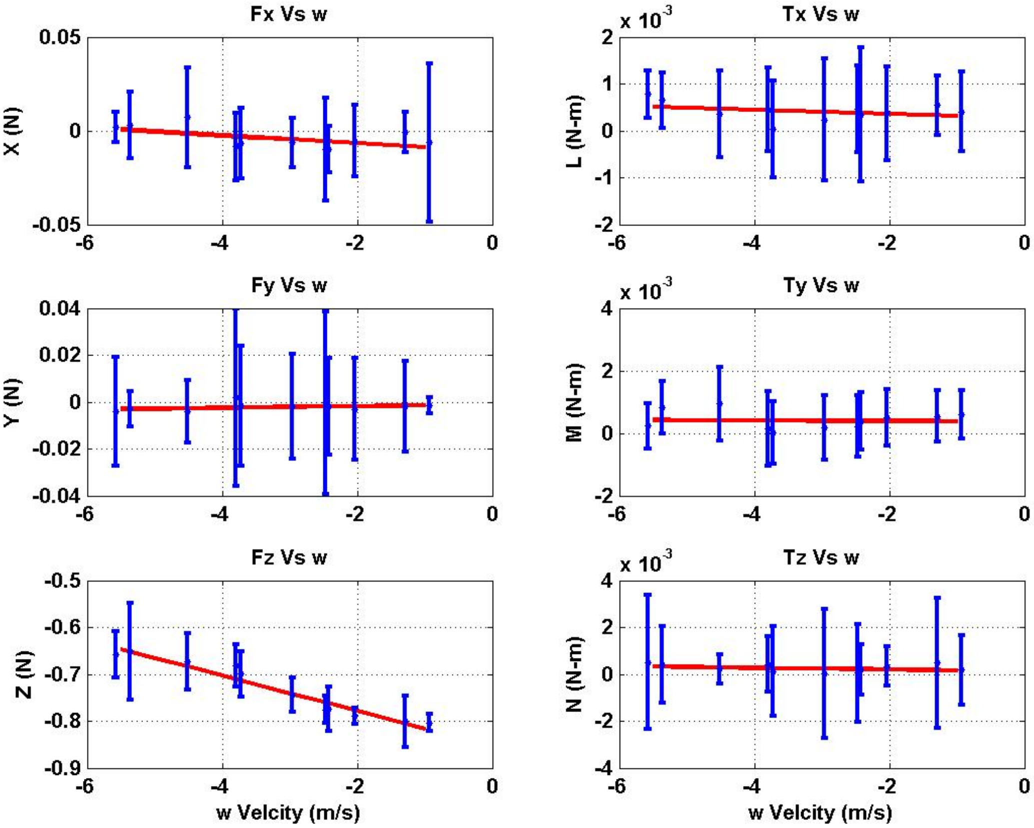

Figure 3.11: Vehicle Loading Due to w Velocity Component

Stability Derivative	Parameter	% Error Fit
X_w	-0.0301	26.3286
Y_w	0.0051	25.7114
Z_w	-0.5371	8.8420
L_w	-0.7053	24.1293
M_w	-0.1286	30.2218
N_w	-0.2867	31.8211

Table 3.4: w Stability Derivatives

3.3.5 Experimental Setup for Rotational Stability Derivatives

This section will describe the test setup for collecting data from the rotational stability derivatives. This differs from the previous section, due to the challenge of producing and measuring accurately a rotational disturbance. Another solution is to rotate the vehicle about its principle axes. Having the vehicle rotate in “still” air is equivalent to the microquad encountering a rotational disturbance, because there is a relative rotation between the air and the vehicle. Here the data processing is more intense, but achieves the same result of getting rotation stability derivatives.

The initial setup is similar to the previous section as shown in Figure 3.12, where the microquad is rigidly mounted to a 6-axis F/T sensor as described in §3.3.2. This configuration can rotate the vehicle about either the x_b or y_b body axis, depending on the orientation in which the vehicle is attached. For a r rate, the vehicle is rotated about the z_b axis, this configuration is depicted in Figure 3.13. The apparatus is designed to rotate about the vehicle's principle axis. This rotation is driven by a Hi-Tec$^{\text{TM}}$ servo which is actuated through the Labview$^{\text{TM}}$ interface. Servos operate like a stepper motor where a PWM signal determines the position. Originally, the servo was commanded steps to obtain the desired rotation rate, which resulted in a staircase start and stop motion throughout the rotation, which is ill-desired. The solution was to start with 0% duty cycle, then step to a 100% duty cycle. This resulted in a smooth 180° rotation from the starting position to the ending position. The rate is controlled by changing the voltage supplied to the servo motor. A low voltage source results in a slower rotation rate, while increasing the voltage supply increases the rotation rate.

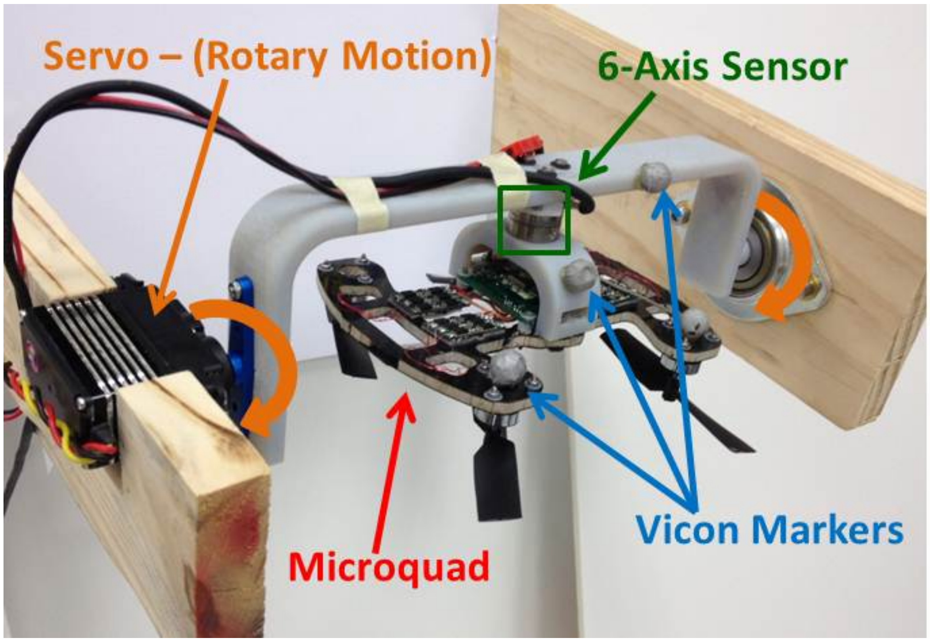

Figure 3.12: Setup for Simulating p and q Rotational Disturbances

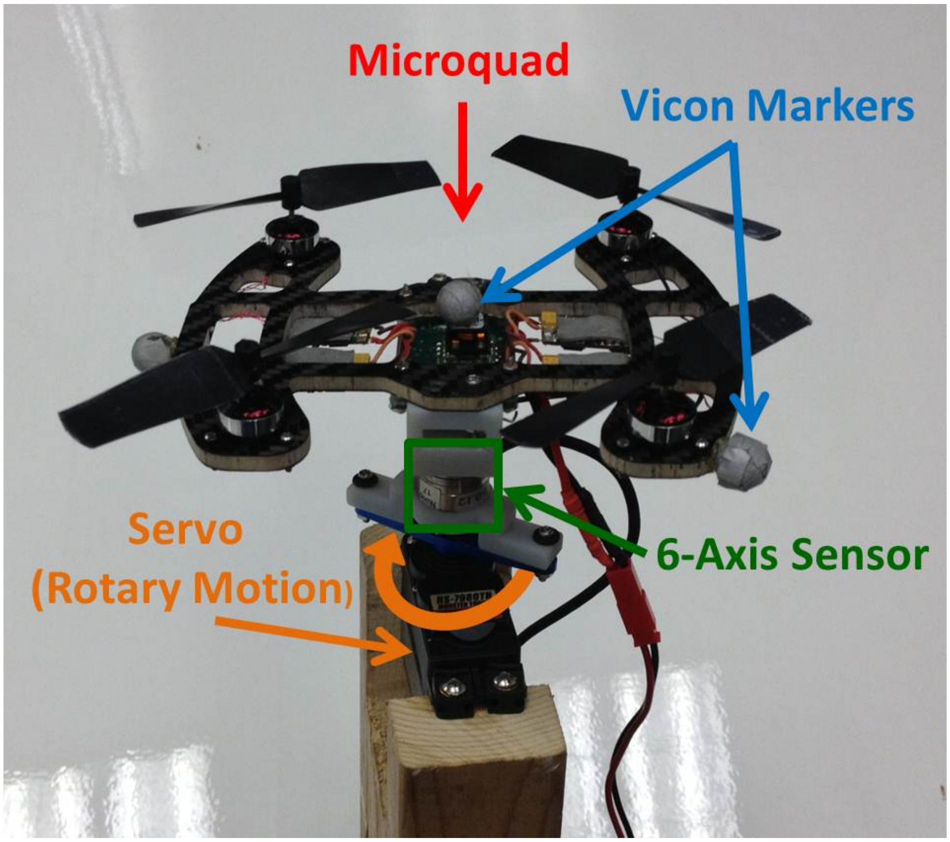

Figure 3.13: Setup for Simulating r Rotational Disturbances

The rotation of the vehicle is tracked by a motion caption system developed by Vicon$^{\text{TM}}$. A Vicon$^{\text{TM}}$ system is a network of cameras that track reflective markers. All the cameras are synced together. Each individual camera has an array of LEDs that strobe at a given frequency, in this case 100 Hz, which matches to the frame rate of the cameras. The light produced by the strobe hits a reflective marker and is bounced into the camera, where a light filter only allows the wavelength of the LED light pass through to illuminate the CCD of the camera. To determine the position of the marker, a calibration procedure is required. This is accomplished by the Tracker$^{\text{TM}}$ software, which determines the relative position of one camera to another. The capture volume is then oriented to a desired coordinate system in the room by placing the calibration wand in the desired location. This defines the origin of the control volume. During each strobe illumination, the software computes the position of each marker the system detects. A cluster with a minimum of 3 markers in a known pattern represents a body; therefore, the position and orientation of the object is calculated. An example of this is seen in Figure 3.14. All data computed by Tracker$^{\text{TM}}$ is streamed via an Ethernet cable to the computer operating Labview$^{\text{TM}}$ code developed for this test configuration. The data is time stamped, so a rate is able to be calculated.

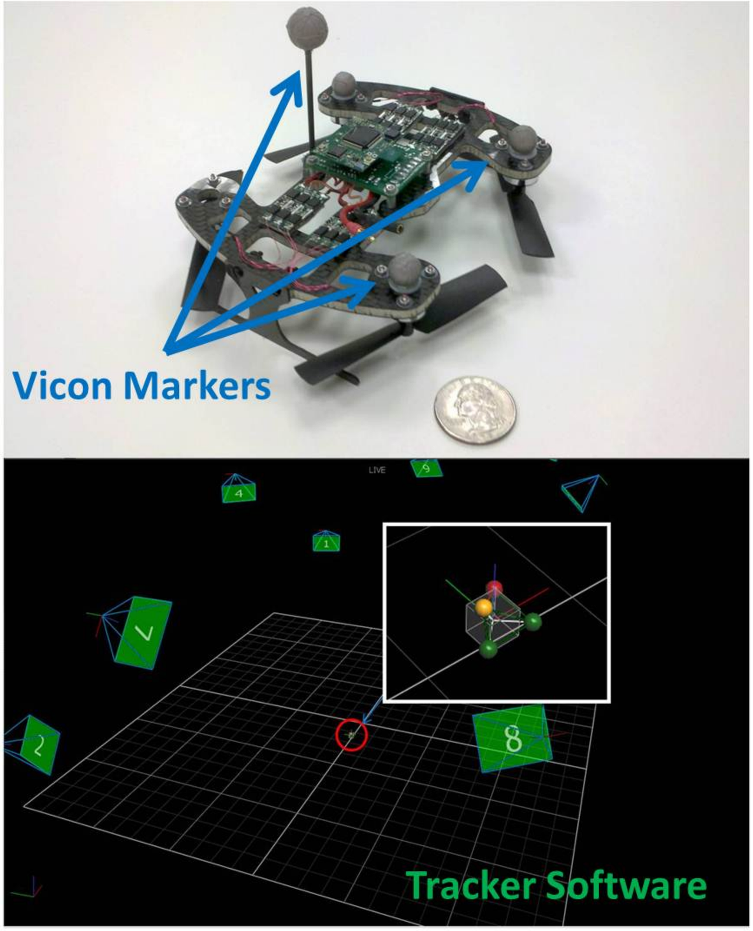

Figure 3.14: Vicon^{TM} Markers Placed on the Vehicle, and Tracker^{TM} Software Environment

3.3.6 Data Processing for Rotational Components

This section describes the process for data reduction for the rotational stability derivatives. Once the data is collected, the force and moment data is first filtered as described in §3.3.3, then re-sampled to sync with the motion capture data generated from Vicon^{TM}. This is easily accomplished using Matlab^{TM}'s ‘interp1’ function. Typically, the motion capture data and F/T sensor measurements are misaligned due to delays in recording these measurements, but in this case these values consistently showed about 100 ms delay between the two data sets. This is due to the F/T data being recorded on the DAQ board in a buffer, then being dumped to a data file in Labview^{TM}, while the motion capture data was being streamed from a second computer. To align the sets, both motion capture data and F/T data were normalized and the bias removed. The distinct spike at the start of each rotation in both the motion capture data and in the corresponding moment data made aligning the two data sets effortless. Once data sets were aligned, the data was truncated to provide 3 data sets for each rotation rate. This shows that each test is repeatable.

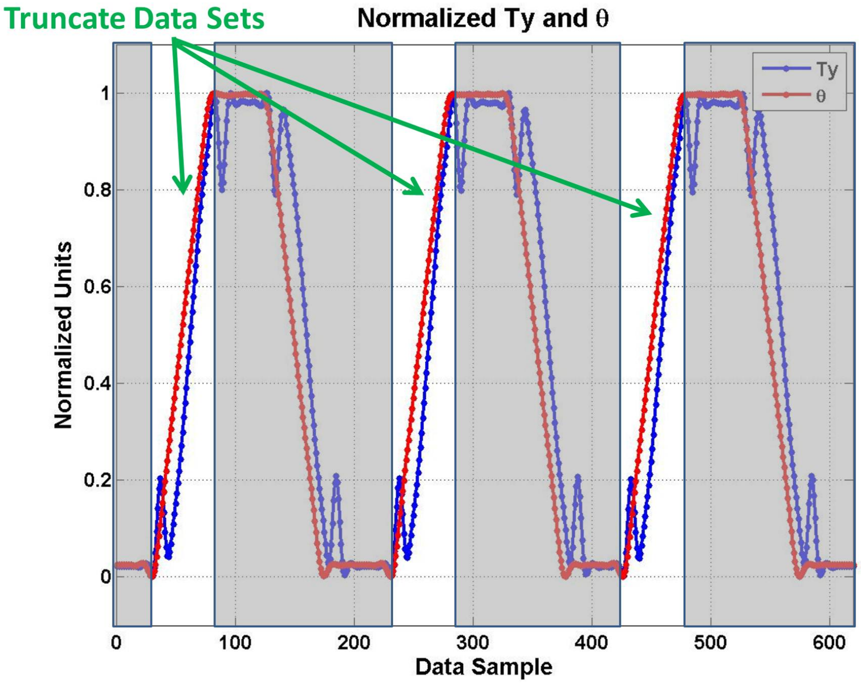

Figure 3.15: Example of Truncating Rotational Data Sets

Due to the F/T sensor not being on the vehicle's CG, as illustrated in Figure 3.4, this needs to be accounted for in the data reduction process. For example, for a q rotation rate, an $mg\sin\theta$ is subtracted from the X-force and for N moment, a $lmg\sin\theta$ is subtracted from the torque measurement about the y_b-axis. The results from this provides a fairly constant force and torque for a constant rotation rate. An example of this is seen in Figure 3.16 and accounts for the different coordinate systems. It should be noted that the data is normally truncated further to ignore the starting and stopping effects from the rotation. Once this is completed for every data set, each set is averaged, providing 3 data points for each rotation rate. This process is repeated several times to find a linear trend that are used for determining the stability derivative.

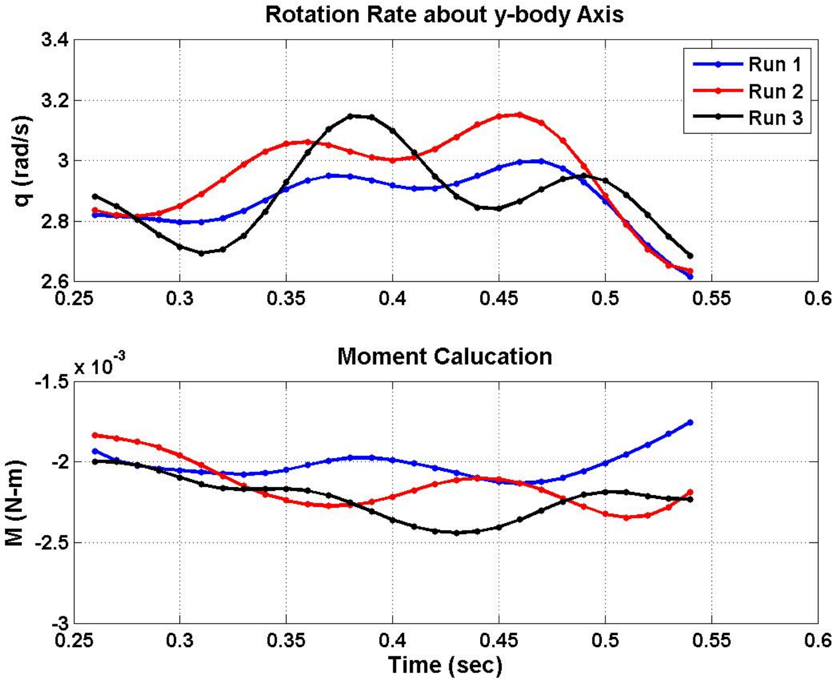

Figure 3.16: Post-Process Data Set from a Rotational Disturbance

3.3.7 Results For Rotational Stability Derivatives

After the data is processed, it yields similar graphs found in § 3.3.4. The same approached used in § 3.3.4 yield stability derivatives for the rotational states. For a p rate, which is a rotation about the x_b-axis of the vehicle, the results are seen in Figure 3.17 and Table 3.5. There is a strong linear relationship between F_y and T_x, which is to be expected with a rotation about the x_b-axis. The result of this parameter has a fairly large scatter, indicated by the percent error fit. These terms will be ignored, as they show a weak linear relationship to a q rate. A rotation about the y_b-axis corresponds to a q body rate. Here there is a strong linear relationship for F_x and T_y, similar to the p body rate. This is expected as the vehicle is symmetric and should therefore yield similar results. Again, the other parameters show a weak linear relationship to a p body rate. The results are shown in Figure 3.18 and Table 3.6. For the r body rate, which is about the z_b-axis, the only significant parameter is T_z. This is reflected in Figure 3.19. The remaining parameters show a weak linear relation to the r body rate. This is reinforced by Table 3.7, as the other parameters have high percent fit errors.

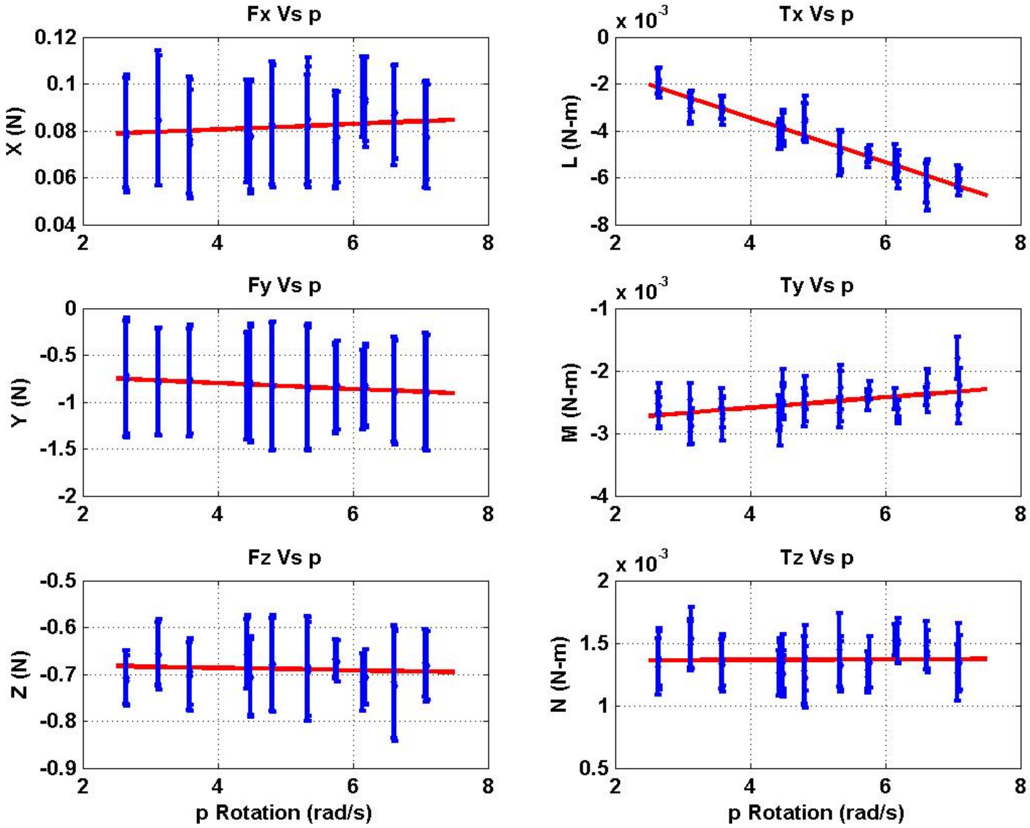

Figure 3.17: Vehicle Loading Due to p Rotational Component

Stability Derivative	Parameter	% Error Fit
X_p	0.0168	24.3065
Y_p	-0.4496	9.5037
Z_p	-0.0363	28.6406
L_p	-15.8465	7.0356
M_p	1.4214	17.0019
N_p	0.0169	28.5317

Table 3.5: p Stability Derivatives

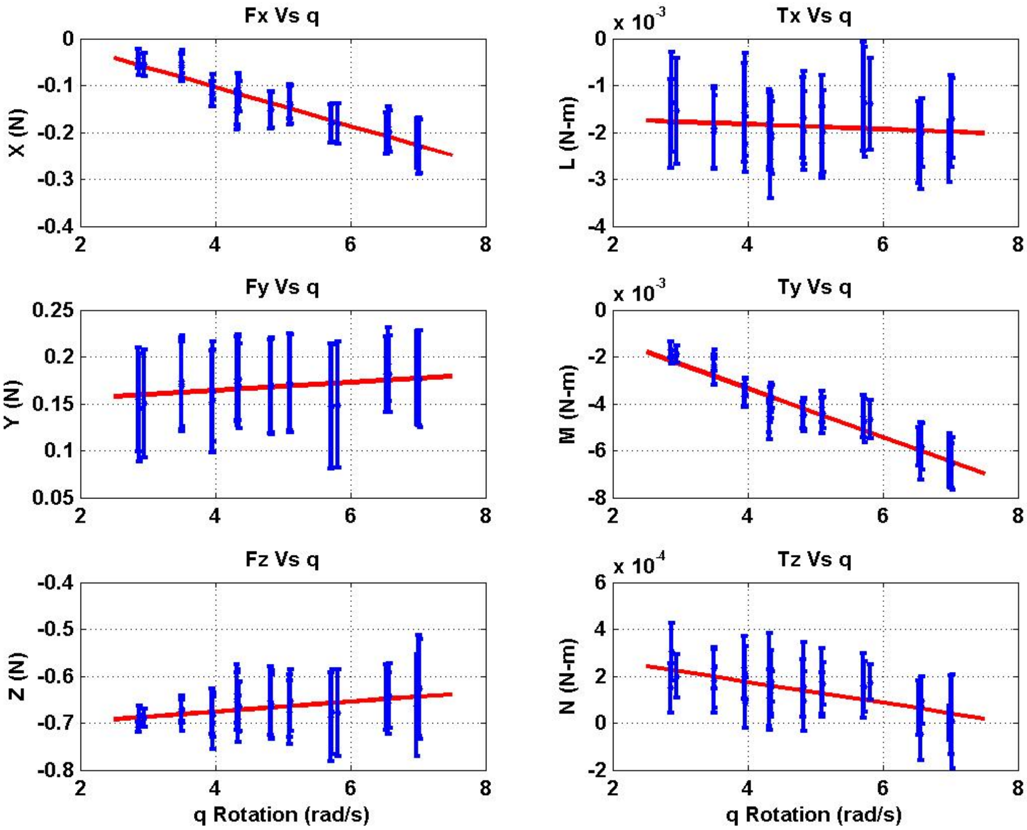

Figure 3.18: Vehicle Loading Due to q Rotational Component

Stability Derivative	Parameter	% Error Fit
X_q	-0.6005	9.1727
Y_q	0.0614	23.3858
Z_q	0.1528	18.3435
L_q	-0.8858	25.2096
M_q	-17.3849	7.9364
N_q	-0.3752	13.7467

Table 3.6: q Stability Derivatives

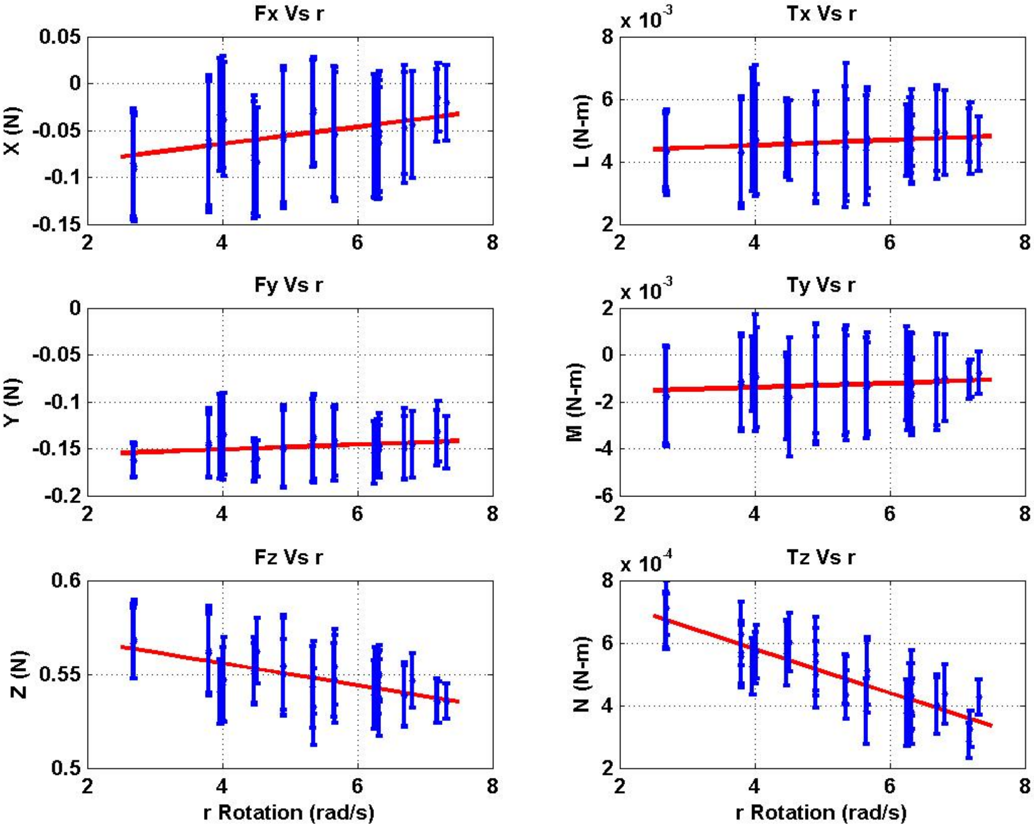

Figure 3.19: Vehicle Loading Due to r Rotational Component

Stability Derivative	Parameter	% Error Fit
X_r	0.1315	20.7173
Y_r	0.0375	24.7293
Z_r	-0.0851	16.9127
L_r	1.3798	27.8799
M_r	1.5030	27.5254
N_r	-0.5845	9.5657

Table 3.7: r Stability Derivatives

3.3.8 Final Results for Full Linear Model

Combining the results described in this chapter with the results from the system identification performed by Miller [15] as explained in section§3.2, yields the full linear model with a disturbance model. For the disturbance matrix **D**, the negative of the stability derivatives found in the above sections make up the linear parameters of this matrix. These “disturbance” derivatives are denoted with a subscript g. Any parameter having a percent fit error larger than 10% indicated a weak linear relationship for that parameter, therefore will be ignored. The resulting model is shown in Equation 3.9 with the parameters reflected in Table 3.8.

$$\dot{\vec{x}} = \mathbf{A}\vec{x} + \mathbf{B}\vec{u} + \mathbf{D}\vec{d} \tag{3.8}$$

$$\begin{Bmatrix} \dot{u} \\ \dot{v} \\ \dot{w} \\ \dot{p} \\ \dot{q} \\ \dot{r} \\ \dot{\phi} \\ \dot{\theta} \\ \dot{\psi} \end{Bmatrix} = \begin{bmatrix} X_u & 0 & 0 & 0 & X_q & 0 & 0 & -g & 0 \\ 0 & Y_v & 0 & Y_p & 0 & 0 & g & 0 & 0 \\ 0 & 0 & Z_w & 0 & 0 & 0 & 0 & 0 & 0 \\ 0 & L_v & 0 & L_p & 0 & 0 & L_\phi & 0 & 0 \\ M_u & 0 & 0 & 0 & M_q & 0 & 0 & M_\theta & 0 \\ 0 & 0 & 0 & 0 & 0 & N_r & 0 & 0 & 0 \\ 0 & 0 & 0 & \phi_p & 0 & 0 & 0 & 0 & 0 \\ 0 & 0 & 0 & 0 & \theta_q & 0 & 0 & 0 & 0 \\ 0 & 0 & 0 & 0 & 0 & \psi_r & 0 & 0 & 0 \end{bmatrix} \begin{Bmatrix} u \\ v \\ w \\ p \\ q \\ r \\ \phi \\ \theta \\ \psi \end{Bmatrix} + \begin{bmatrix} 0 & 0 & 0 & 0 \\ 0 & 0 & 0 & 0 \\ 0 & 0 & 0 & Z_{thr} \\ 0 & L_{lat} & 0 & 0 \\ M_{lon} & 0 & 0 & 0 \\ 0 & 0 & N_{yaw} & 0 \\ 0 & 0 & 0 & 0 \\ 0 & 0 & 0 & 0 \\ 0 & 0 & 0 & 0 \end{bmatrix} \begin{Bmatrix} \delta_{lon} \\ \delta_{lat} \\ \delta_{yaw} \\ \delta_{thr} \end{Bmatrix}$$

$$+ \begin{bmatrix} X_{u_g} & 0 & 0 & 0 & X_{q_g} & 0 \\ 0 & Y_{v_g} & 0 & Y_{p_g} & 0 & 0 \\ 0 & 0 & Z_{w_g} & 0 & 0 & 0 \\ 0 & L_{v_g} & 0 & L_{p_g} & 0 & 0 \\ M_{u_g} & 0 & 0 & 0 & M_{q_g} & 0 \\ 0 & 0 & 0 & 0 & 0 & N_{r_g} \\ 0 & 0 & 0 & 0 & 0 & 0 \\ 0 & 0 & 0 & 0 & 0 & 0 \\ 0 & 0 & 0 & 0 & 0 & 0 \end{bmatrix} \begin{Bmatrix} d_u \\ d_v \\ d_w \\ d_p \\ d_q \\ d_r \end{Bmatrix} \tag{3.9}$$

Parameter	Value	Parameter	value	Parameter	value	Parameter	value
X_u	-0.4425	X_q	0.0169	M_{lon}	0.6944	Y_{p_g}	0.4496
M_u	19.5699	M_q	8.8773	L_{lat}	0.5436	L_{p_g}	15.8465
Y_v	-0.8201	N_r	-0.7578	N_{yaw}	0.1117	X_{q_g}	0.6005
L_v	-7.7109	Y_ϕ	8.023	Z_{thr}	-0.014	M_{q_g}	17.3849
Z_w	-0.5164	L_ϕ	4.5387	X_{u_g}	0.4703	N_{r_g}	0.5845
Y_p	0.0169	X_θ	-9.2773	Y_{v_g}	0.4712	-	-
L_p	0.4305	M_θ	-27.6411	Z_{w_g}	0.5371	-	-

Table 3.8: Complete Table of Stability, Control and Disturbance Derivatives

3.3.9 Actuator Response

When controlling both body dynamics and disturbance rejection, actuator response becomes an important attribute. An accurate model of the actuator dynamics can aid in simulation and control design. Typically, actuators roll off at a high frequency, making it important to understand at what frequency this occurs. Modeling the actuator response for the microquad is straightforward, since all actuation is directly controlled by the motors. To identify a model for the motor response a similar experimental setup as seen in Figure 3.4 is used. The motor response is ascertained by commanding a throttle chirp input that sweeps from 0 Hz to 15 Hz about the nominal command of 60% throttle with an amplitude of 15% throttle. This is completed over a duration of 20 seconds. Data is acquired at 100 Hz – which captures the motor command and F_z force. The mean command and force measurements were subtracted out of the data for identification purposes; doing so illuminates how the motor magnitude and phase change with frequency.

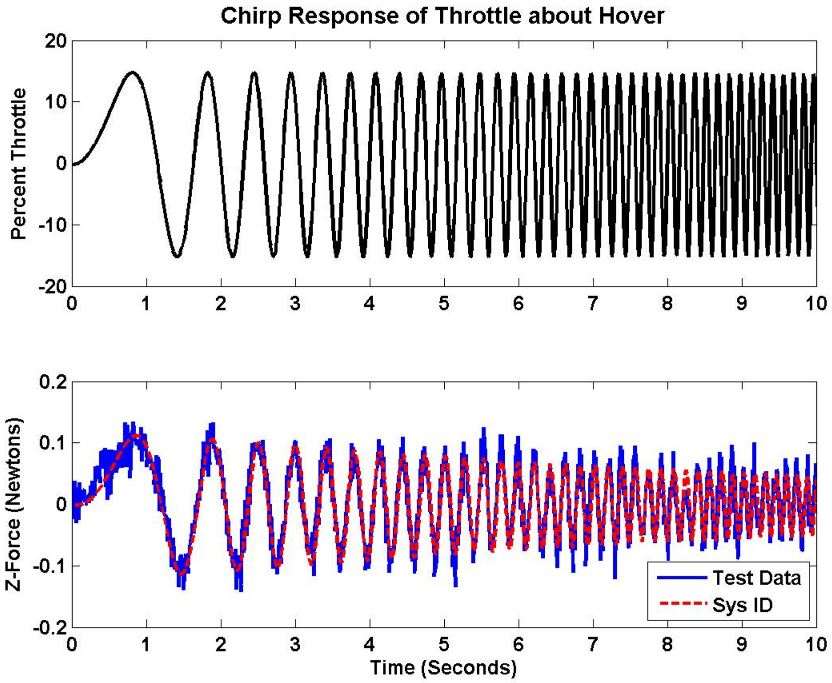

Figure 3.20: Motor Response to a Chirp Input

Once the mean is subtracted, Matlab$^{\text{TM}}$'s ‘ident’ toolbox is used for spectral analysis. First, a spectral model was generated from the data, also known as a bode plot. This provides an input-output relationship for the command-to-force measurements. In order to estimate the spectral model, the ‘SPAFDR’ function is used. Once this is completed, the structure of the model is determined by the shape the spectral plot. A single pole transfer function emulates the shape of the motor response. Next, the ‘Process Model’ function is used to determine the parameters for the first order model, which is reflected in Equation 3.11. Finally the coherence is computed 3.10 from [6],where Φ_{uu} and Φ_{yy} are autocorrelations and Φ_{uy} is the cross-correlation between the input and output. This provides a measure for the validity of the model at a given frequency, with 1 indicating it is 100% correlated, and 0 indicating there is no correlation. The experiment correlated fairly well up to 10 HZ, at which point the magnitude began to drop off considerably. The spectral data, identified motor model, and coherence is all reflected in Figure 3.21.

$$\gamma_{uy}^2(\omega) = \frac{|\Phi_{uy}(\omega)|^2}{|\Phi_{uu}(\omega)||\Phi_{yy}(\omega)|} \tag{3.10}$$

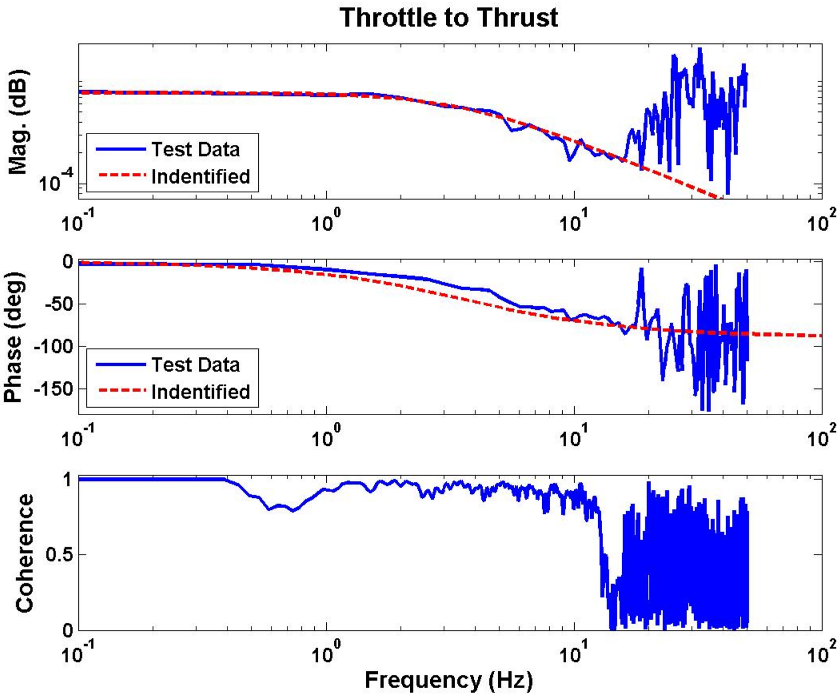

Figure 3.21: Bode Plot for Motor Response

$$\frac{Z_{thr}}{\delta_{thr}} = \frac{0.0007704}{0.04429s + 1} \tag{3.11}$$

Chapter 4

Vehicle Analysis

4.1 Overview

Now that a linear model has been established for the microquad, its disturbance properties can be analyzed. The analysis tools presented here require a stable system. If a vehicle is naturally stable, then the bare air frame dynamics can be examined independent of control, which is desirable. Unfortunately, most agile vehicles at this scale are inherently unstable. They often require a fast inner-loop control scheme to stabilize the attitude dynamics of the vehicle. The outer-loop is typically intended for the position control of the vehicle in space, which is more closely associated with disturbance rejection. Therefore, it is reasonable to look at the closed inner-loop system when applying these analysis techniques. These are ideal techniques because every system has limitation regardless of the control scheme. These types of techniques are valuable because they provide insight on the vehicle strengths and weaknesses – vital information when comparing multiple platforms.

4.2 Control Design

This section will discuss the system structure formulation for the inner and outer loops of the microqrad. The inner-loop dynamics pertain to the attitude of the vehicle and require a higher bandwidth than the outer-loop dynamics. Outer-loop dynamics deal with position and/or velocity of the vehicle, as well as heading. The inner-loop dynamics are faster than those of the outer-loop, which is why sensors such as rate gyros and accelerometers are useful for maintaining inner-loop stability. Sensors like these possess fast update rates. For the outer-loop, lower sensing is adequate and is typically provided by GPS measurements; however, in this case it is provided by Vicon$^{\text{TM}}$.

Control design for the microquad has been explored and analyzed by Miller [15]. This section will provide a basic overview of controller design and structure, but will not go into detail of the complete development. If more details are needed, refer to [15].

4.3 Static $\mathcal{H}_\infty$

Control designs of the microquad were heavily explored by Miller [15], but are laid out here in a brief outline. There are several control design methods that can be applied to any system, but the most useful for flight dynamics simulation are outlined in [10]. Due to limited on board computing, it is important to implement a static gain controller. Since the vehicle is fairly uncoupled, the model can be reduced to a Single Input Single Output (SISO) control design. There are a lot of analysis tools for SISO systems, making this is an attractive method. Another route is Linear Quadratic Gaussian (LGQ) method, which is a more complicated control structure that employs a linear estimator, a Kalman Filter, which will provide an estimate for all the states in the model. This is very useful, as are most systems that provide a limited number of measurements, but this requires powerful processors, which cannot be afforded at this scale. Once an estimation of the states is known, then a Linear Quadratic Regular (LQR) is used to finish the control design. This is ideal for Multiple Input Multiple Output (MIMO) systems. One of the limitations of the LQR controller is that it requires full state feedback; hence it is coupled with a LQG estimator. However, Levine and Athans [21] came up with a solution, deemed Output LQR, for designing a controller using the LQR framework with just the output measurements. This allows static feedback control to be implemented. More modern techniques of $\mathcal{H}_\infty$ design also require large computing power, since the compensator usually has dynamics associated with it. $\mathcal{H}_\infty$ designs are highly desirable because they are able to incorporate model uncertainty to add robustness to the system. $\mathcal{H}_\infty$ tends to have good disturbance rejection properties. A Static $\mathcal{H}_\infty$ method was developed by Gadewadikar [19]. This method possesses the attributes $\mathcal{H}_\infty$ control design, in addition to possessing a simplistic static feedback controller. This is easy to implement and ideal for platforms at this scale. For this paper, only the static $\mathcal{H}_\infty$ controller will be considered.

The goal of static $\mathcal{H}_\infty$ is to extend the concepts of $\mathcal{H}_\infty$ design to static feedback framework.

One advantage of this control design is that it boasts good disturbance rejection properties. The algorithm does not require an initial stabilizing gain, which other methods such as output LQR requires. Figure 4.1 shows the basic framework for the $\mathcal{H}_\infty$ structure. The basic principle of the control design is to minimize the signal $\vec{z}$ from exogenous inputs, in this case external atmospheric disturbances $\vec{d}$. To minimize the signal $\vec{z}$, a quadratic function is formulated with both the states $\vec{x}$ and the control inputs $\vec{u}$; where $\mathbf{Q}$ is a positive definite weighting matrix for the states, and $\mathbf{R}$ is a positive definite weighting matrix for the control inputs. These weighting matrices can be thought of as control knobs, intended to emphasize reducing state fluctuation or limit control energy for a specific control input.

$$\begin{aligned} \dot{\vec{x}} &= \mathbf{A}\vec{x} + \mathbf{B}\vec{u} + \mathbf{D}\vec{d} \\ \dot{\vec{y}} &= \mathbf{C}\vec{x} \end{aligned} \tag{4.1}$$

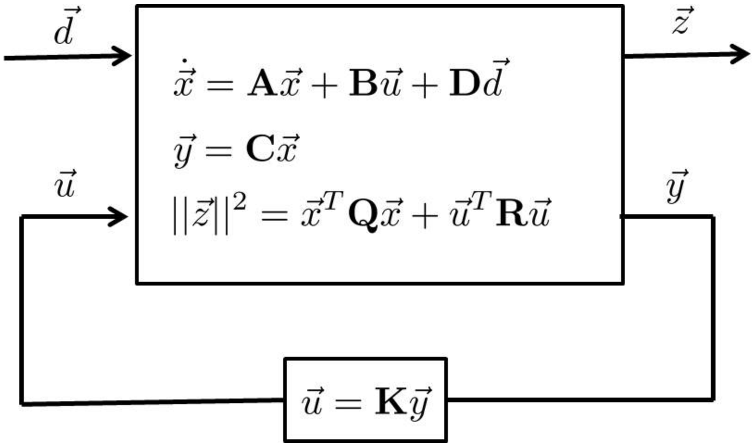

Figure 4.1: $\mathcal{H}_\infty$ Framework

There are several necessary and sufficient conditions outlined in [18]. A quick summary of those conditions will be stated here using the LTI model repeated in Equation 4.1. The pair $(\mathbf{A}, \mathbf{B})$ needs to be stabilizable, meaning there exists a $\mathbf{K}$ such that $\mathbf{A} - \mathbf{BK}$ is asymptotically stable. The pair $(\mathbf{A}, \mathbf{C})$ is detectable, meaning there exists a $\mathbf{L}$ such that $\mathbf{A} - \mathbf{LC}$ is stable. Most importantly the system is said to be output stabilizable if $\mathbf{A} - \mathbf{BKC}$ is stable. Finally, the system is bounded by γ if Equation 4.2 is satisfied.

$$\frac{||\vec{z}(t)||_2^2}{||\vec{d}(t)||_2^2} = \frac{\int_0^\infty ||\vec{z}(t)||^2 \mathrm{d}t}{\int_0^\infty ||\vec{d}(t)||^2 \mathrm{d}t} = \frac{\int_0^\infty \left(\vec{x}^T \mathbf{Q} \vec{x} + \vec{u}^T \mathbf{R} \vec{u}\right) \mathrm{d}t}{\int_0^\infty \vec{d}^T \vec{d} \mathrm{d}t} \leq \gamma^2 \tag{4.2}$$

Once these conditions are met, then an optimal gain can be determined. The steps below outline the algorithm [18], which centers around well-known algebraic Riccati equations.

Step 1:

Initialize Parameters.

- Set: $n = 0$, $L_0 = 0$
- Select weighting matrices $\mathbf{Q}$, $\mathbf{R}$, and the bound γ.

Step 2:

n^{th} iteration step:

- Solve Riccati equation for $\mathbf{P}_n$

  $\mathbf{A}^T \mathbf{P}_n + \mathbf{P}_n \mathbf{A}^T + \mathbf{Q} - \mathbf{P}_n \mathbf{B} \mathbf{R}^{-1} \mathbf{B}^T \mathbf{P}_n + \frac{1}{\gamma^2} \mathbf{P}_n \mathbf{D} \mathbf{D}^T \mathbf{P}_n + \mathbf{L}_n^T \mathbf{R}^{-1} \mathbf{L}_n$
- Evaluate the gain, $\mathbf{K}$ and update $\mathbf{L}$:
  - $\mathbf{K}_{n+1} = \mathbf{R}^{-1} \left(\mathbf{B}^T \mathbf{P}_n + \mathbf{L}_n\right) \mathbf{C}^T \left(\mathbf{R} \mathbf{K}_{n+1} \mathbf{C} - \mathbf{B}^T \mathbf{P}_n\right)$
  - $\mathbf{L}_{n+1} = \mathbf{R} \mathbf{K}_{n+1} \mathbf{C} - \mathbf{B}^T \mathbf{P}_n$
- if $||\mathbf{K}_{n+1} - \mathbf{K}_n||_F$ (Frobenius Norm of $\Delta \mathbf{K}$) within tolerance, proceed to Step 3, otherwise update $n = n + 1$ and repeat Step 2.

Step 3:

Terminate.

- Set $\mathbf{K}^* = \mathbf{K}_{n+1}$

This algorithm is easily implemented using Matlab$^{\text{TM}}$'s well understood Riccati equations. This provides an optimal $\mathbf{K}^*$ in the framework provided above. Once the basic framework is in place, the weighting matrices are easily tweaked until the desired performance is achieved. This control design technique will be used throughout the rest of the control design process.

4.4 Inner-Loop Control Structure

The inner-loop focuses on regulating the attitude of the vehicle. A schematic of the system is seen in Figure 4.2. Here, the matrices in Equation 3.9 will be partitioned in a manner aimed at focusing on the inner-loop dynamics. For the inner-loop, the following states are included in the model $\vec{x} = [u, v, w, p, q, r, \phi, \theta]^T$, with control inputs of $\vec{u} = [\delta_{lon}, \delta_{lat}, \delta_{yaw}]^T$, and the GINA mote providing measurements $y = [\hat{\phi}, \hat{\theta}, \hat{p}, \hat{q}, \hat{r}]^T$. The outer-loop control design will focus on heading ψ and position $[x, y, z]^T$. In later sections, this model will be partitioned further to help illustrate the usefulness of analysis tools developed here. For example, the model can be reduced to include only the longitudinal states $[u, q, \theta]$.

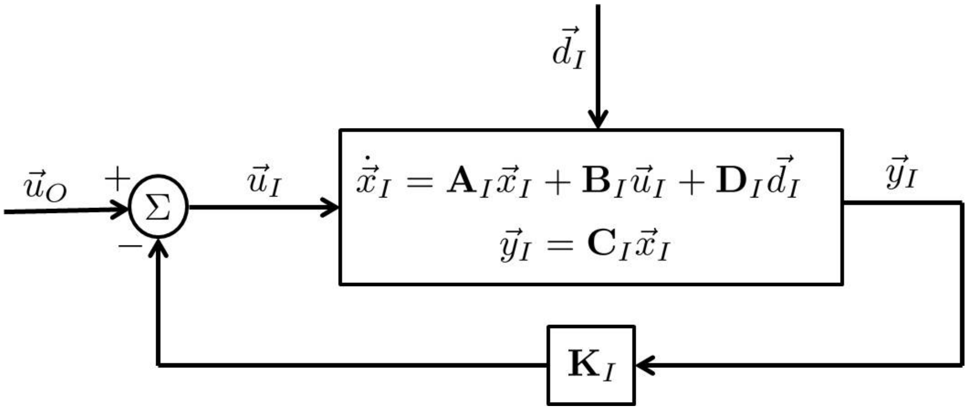

Figure 4.2: Inner-Loop of Microquad

Using the model from Chapter 3 § 3.9 and the following weighting matrices seen in Equations 4.3 and 4.4 from Miller [15], the static $\mathcal{H}_\infty$ control algorithm can be applied.

$$\mathbf{Q_i} = \begin{bmatrix} 0.005 & 0 & 0 & 0 & 0 & 0 & 0 & 0 \\ 0 & 0.01 & 0 & 0 & 0 & 0 & 0 & 0 \\ 0 & 0 & 500 & 0 & 0 & 0 & 0 & 0 \\ 0 & 0 & 0 & 50 & 0 & 0 & 0 & 0 \\ 0 & 0 & 0 & 0 & 50 & 0 & 0 & 0 \\ 0 & 0 & 0 & 0 & 0 & 1500 & 0 & 0 \\ 0 & 0 & 0 & 0 & 0 & 0 & 0.05 & 0 \\ 0 & 0 & 0 & 0 & 0 & 0 & 0 & 0.05 \end{bmatrix} \tag{4.3}$$

$$\mathbf{R_i} = \begin{bmatrix} 100 & 0 & 0 \\ 0 & 200 & 0 \\ 0 & 0 & 0.2 \end{bmatrix} \tag{4.4}$$

The static $\mathcal{H}_\infty$ algorithm yields a feedback gain matrix shown in 4.5. The closed-loop $\mathbf{A}$ matrix is calculated by $\mathbf{A}_{CL} = \mathbf{A} - \mathbf{BKC}$.

$$\mathbf{K} = \begin{bmatrix} 0 & 1.825 & 0 & 0.937 & 0 \\ 1.916 & 0 & 0.901 & 0 & 0 \\ 0 & 0 & 0 & 0 & 1.768 \end{bmatrix} \tag{4.5}$$

4.5 Outer-Loop Control Structure

Once control for the inner-loop is attained, the next step is to construct the outer-loop model. The basic outer-loop structure is represented by the block diagram shown in Figure 4.3. The outer-loop states are $\vec{x} = [u, v, w, p, q, r, \phi, \theta, \psi, x, y, z]^T$, with the controls being $\vec{u} = [\delta_{lon}, \delta_{lat}, \delta_{yaw}, \delta_{thr}]^T$. Finally the measured states are $y = [\hat{x}, \hat{y}, \hat{z}, \hat{u}, \hat{v}, \hat{w}, \hat{\psi}]^T$. These values are attained from the Vicon$^{\text{TM}}$ system. The outer-loop-control infrastructure is implemented in Labview$^{\text{TM}}$ software. Again, the static $\mathcal{H}_\infty$ control design procedure is used to calculate the static gains for the system.

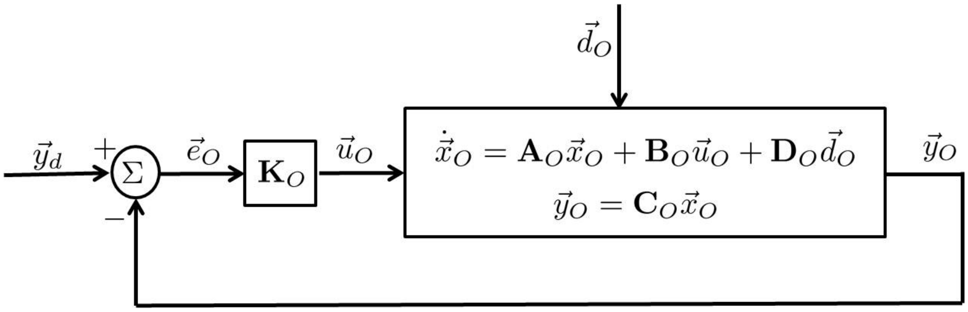

Figure 4.3: Outer-Loop of Microquad

To account for the extra states, $\vec{x} = [\psi, x, y, z]^T$. These states are in the inertial frame and are approximated by setting them equal to their body frame counterparts, as seen in Equations 4.6. This is a common approximation with small perturbation models [12].

$$\begin{aligned}\dot{\psi} &= r\\ \dot{x} &= u\\ \dot{y} &= v\\ \dot{z} &= w\end{aligned} \tag{4.6}$$

To achieve these states integrators are added into the system with matrix **F** 4.7, which is concatenated with the inner close-loop matrix, $\mathbf{A}_{CL}$ shown in Equation 4.8.

$$\mathbf{F} = \begin{bmatrix} 0 & 0 & 0 & 0 & 0 & 1 & 0 & 0 \\ 1 & 0 & 0 & 0 & 0 & 0 & 0 & 0 \\ 0 & 1 & 0 & 0 & 0 & 0 & 0 & 0 \\ 0 & 0 & 1 & 0 & 0 & 0 & 0 & 0 \end{bmatrix} \tag{4.7}$$

$$\mathbf{A}_o = \begin{bmatrix} \mathbf{A}_{CL} & \mathbf{0} \\ \mathbf{F} & \mathbf{0} \end{bmatrix} \tag{4.8}$$

Once the outer-loop matrices are constructed, the following weighting matrices were selected 4.9 and 4.10 from Miller [15].

$$\mathbf{Q_o} = diag\begin{bmatrix} 7.5 & 15 & 150 & 0.075 & 0.075 & 0.0225 & 0.75 & 0.75 & 75 & 1500 & 1500 & 75 \end{bmatrix} \tag{4.9}$$

$$\mathbf{R_o} = \begin{bmatrix} 0.5000 & 0 & 0 & 0 \\ 0 & 0.5000 & 0 & 0 \\ 0 & 0 & 0.0010 & 0 \\ 0 & 0 & 0 & 0.0020 \end{bmatrix} \tag{4.10}$$

Now that the frame work is in place to use the static $\mathcal{H}_\infty$ control design, it yields the following outer-loop gain matrix 4.11.

$$\mathbf{K_o} = \begin{bmatrix} -55.2396 & 0 & 0 & -24.5147 & 0 & 0 & 0 \\ 0 & 58.2264 & 0 & 0 & 30.0822 & 0 & 0 \\ 0 & 0 & 0 & 0 & 0 & 0 & 273.8618 \\ 0 & 0 & -193.6882 & 0 & 0 & -285.7285 & 0 \end{bmatrix} \tag{4.11}$$

This gives the basic framework of a model for the microquad. With this model, both analysis and simulation can be performed on the vehicle.

4.6 Gramian Based Analysis

This section will examine controllability (reachability) gramian and demonstrate how this technique can extend to predicting the total disturbance a vehicle is able to reject. This is useful because it provides a method to determine a maximum disturbance loading that a vehicle can encounter in order for it to still be able to return the rates to zero. This is crucial information when determining whether a vehicle is able to operate in a certain environment. First, the reachability gramian will be formulated. This is a useful tool, being that it shows directionality and how easily the state can be reached for a given input [6].

The controllability operator Ψ_c maps the input $u(t)$ at $t = -\infty$ to the final state x_0 at $t = 0$ and is defined for an LTI system in Equation 4.12.

$$\Psi_c : L_2^p(-\infty, 0] \to C^n;\ u \to \int_0^\infty e^{-\mathbf{A}t}\mathbf{B}u(\tau)\mathrm{d}\tau \tag{4.12}$$

Scaling the control input by its maximum control value provides the constraint $||u|| \leq 1$, so the reachable states are defined by the set $\{\Psi_c u \ : \ x_c \in C^n, ||u|| \leq 1\}$. This is equivalent to stating 4.13.

$$\varepsilon_c = \{X_c^{\frac{1}{2}} x_c \ : \ x_c \in C^n, ||x_c|| \leq 1\} \tag{4.13}$$

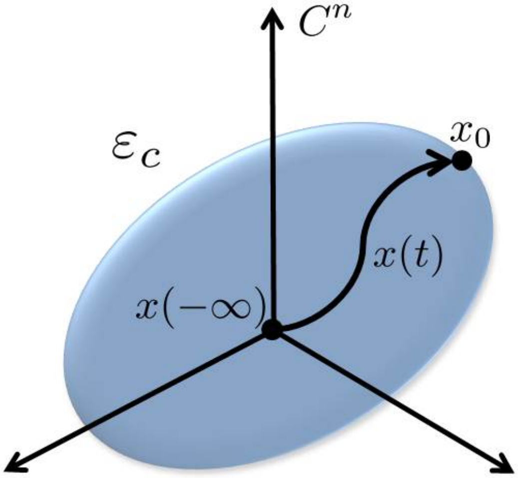

Figure 4.4: Illustration of Reachability Concept

The set 4.13 defines an ellipsoid in C^n space and is illustrated in Figure 4.4, where n is the number of states. X_c is the controllability (reachability) gramian for the pair $(\mathbf{A}, \mathbf{B})$ and is defined in [7], where * denotes the conjugate.

$$X_c = \Psi_c \Psi_c^* = \int_{-\infty}^0 e^{-At}BB^*e^{-A^*t}\mathrm{d}t = \int_{-\infty}^0 e^{At}BB^*e^{A^*t}\mathrm{d}t \tag{4.14}$$

X_c is the solution to the Lyapunov equation. Matlab$^{\mathrm{TM}}$ has a function 'lyap' to solve for X_c. This solution is known as the gramian.

$$AX_c + X_cA^* + BB^* = 0 \tag{4.15}$$

The solution X_c provides information about the system. If $X_c > 0$, it is said X_c is positive definite and the pair $(\mathbf{A}, \mathbf{B})$ is controllable. Taking the Singular Value Decomposition (SVD) of

$X_c^{\frac{1}{2}}$ gives the magnitude and direction of the of the states. The square root of a matrix is found by $Q^{\frac{1}{2}} = U\Lambda^{\frac{1}{2}}U^*$, where Λ is a diagonal matrix of the eigenvalues, and U is matrix of eigenvectors. The SVD is defined by Equation 4.16. While S is a diagonal matrix and gives the magnitude of the principle axes of the ellipsoid, U provides the orientation of the ellipsoid in state space [11].

$$X_c^{\frac{1}{2}} = USV' \tag{4.16}$$

This basic framework is extended to disturbances. The idea is to think of the disturbance in the same manner as a control input. Scaling the disturbance input d by the maximum disturbances expected to be encountered will map which states the vehicle can reach from a given disturbance level. If this disturbance ellipsoid is completely contained within the reachability ellipsoid, then this suggests that the disturbance can be rejected once feedback control is implemented for the outer-loop. This is a powerful tool, owing to the fact it provides the maximum limit for a disturbance acting on a vehicle that it is able to reject. Equation 4.17 is the resulting Lyapunov equation, where X_d is the solution and will be referred to as the distance gramian. Taking the SVD of $X_d^{\frac{1}{2}}$ maps which states can be reached with the equation's given disturbance input.

$$AX_d + X_dA^* + DD^* = 0 \tag{4.17}$$

4.7 Example of Gramian Based Disturbance Analysis

Here we will examine the usefulness of comparing the reachability and disturbance gramian. To illustrate the power of this technique only the longitudinal dynamics will be considered. The model will ignore fluctuation in disturbances; instead using constant wind loading. This model will also not include actuator dynamics. A simple example is being used to clearly illustrate this technique. Equation 4.18 is the LTI model for the longitudinal dynamics. In order to account for the microquad's inherent instability and for this process to work, a stabilizing gain must first be found. The static $\mathcal{H}_\infty$ formulation discussed in §4.3 is used for the controller design. It should be noted that any applicable controller design will apply to this method. The controller itself determines the performance of the vehicle. Therefore, an inner-loop controller would not be required, if the vehicle was inherently stable.

$$\begin{Bmatrix} \dot{u} \\ \dot{q} \\ \dot{\theta} \end{Bmatrix} = \begin{bmatrix} -0.4425 & 0.0169 & -9.2773 \\ 19.5699 & 8.8773 & -27.6411 \\ 0 & 1.0000 & 0 \end{bmatrix} \begin{Bmatrix} u \\ q \\ \theta \end{Bmatrix} + \begin{bmatrix} 0 \\ 0.6944 \\ 0 \end{bmatrix} \begin{Bmatrix} \delta_{lon} \end{Bmatrix} + \begin{bmatrix} 0.4703 & 0.6005 \\ 0 & 17.3849 \\ 0 & 0 \end{bmatrix} \begin{Bmatrix} u_g \\ q_g \end{Bmatrix} \tag{4.18}$$

Using the algorithm outlined in section §4.3, a output stabilizing $\mathbf{K}$ was found using the following weighting matrices $\mathbf{Q} = diag[1, 1, 1]$ and $\mathbf{R} = diag[1]$. The inner closed-loop system can be represented by $\mathbf{A}_{CL} = \mathbf{A} - \mathbf{CKB}$.

$$\mathbf{K} = \begin{bmatrix} 1.4326 & 0.7442 \end{bmatrix} \tag{4.19}$$

Once the inner-loop dynamics are stable, the reachability and distance gramian's can be compared. The goal is to determine the maximum disturbance a given vehicle can reject. It will be seen that this is easily illustrated by plotting the disturbance and reachability ellipsoid against one another. If the disturbance ellipsoid is fully contained within the reachability ellipsoid, then it can be said that the vehicle can adequately reject that disturbance once feedback control is applied. This is verified by implementing a stabilizing outer-loop controller and by using simulations to demonstrate this result.

For the reachability gramian, the control input must be bounded for a $|\vec{u}| < 1$. The model as identified in equation 4.18 control input $\vec{u} \in [-500\ 500]$ for δ_{lon}, δ_{lat}, and δ_{yaw}. For δ_{thr} the control input is $\vec{u} \in [0\ 1000]$. These commands are mixed together to drive each motor. Each motor can receive a command from 0 to 1000 and is the sum of the contribution of each of the $\vec{u} = [\delta_{lon}, \delta_{lat}, \delta_{yaw}, \delta_{thr}]^T$. For hover condition, the vehicle operates around 560 units, leaving 440 units for disturbance and maneuvering. For the gramian, the control input needs to be scaled to 1 or [-1 1] for longitudinal, lateral and yaw control inputs. Here it is chosen that the control saturation limits are [-35 35]. This limiting value of 35 is arbitrary. Once a motor model is introduced, these limits increase and become more realistic. To scale the control matrix to these constraints, the control matrix is multiplied by the absolute value of the saturation limits, in this case $35 * \mathbf{B_{lon}}$. Once this is complete, then the reachability analysis described in §4.6 is performed. The longitudinal dynamics only contain 3 states, making the ellipsoid easy to visualize in 3-dimensional space with the axes being the states.

For the disturbance gramian, two cases will be explored. Similar to the control matrix, the distance matrix is required to be normalized, making $|\vec{d}| < 1$. Here the limit is the maximum constant disturbance the vehicle encounters. In the first case, the disturbance gramian is scaled by $\vec{d}_{max} = [d_{u,max}, d_{q,max}]^T = [4\ m/s, -0.2\ rads/s]$. In this instance, the disturbance ellipsoid is bounded by the reachability ellipsoid, which is shown in Figure 4.5. The 2-D projections of each state are plotted against one another. Clearly, the disturbance ellipsoid is bounded, which predicts that this disturbance can be attenuated. More specifically, in this example, position hold is desired. To attain this, the rates of the vehicle must be brought to zero. The 2-D projection of the rotational rate q and translational velocity u best illustrates this point, as it is seen that the control projection completely contains the disturbance projection. In the second scenario, the disturbance matrix is scaled by $\vec{d}_{max} = [5\ m/s, -0.2\ rads/s]$. Figure 4.6 shows that the distance protruding outside the reachability ellipsoid, which suggests that the vehicle will not reject this disturbance combination.

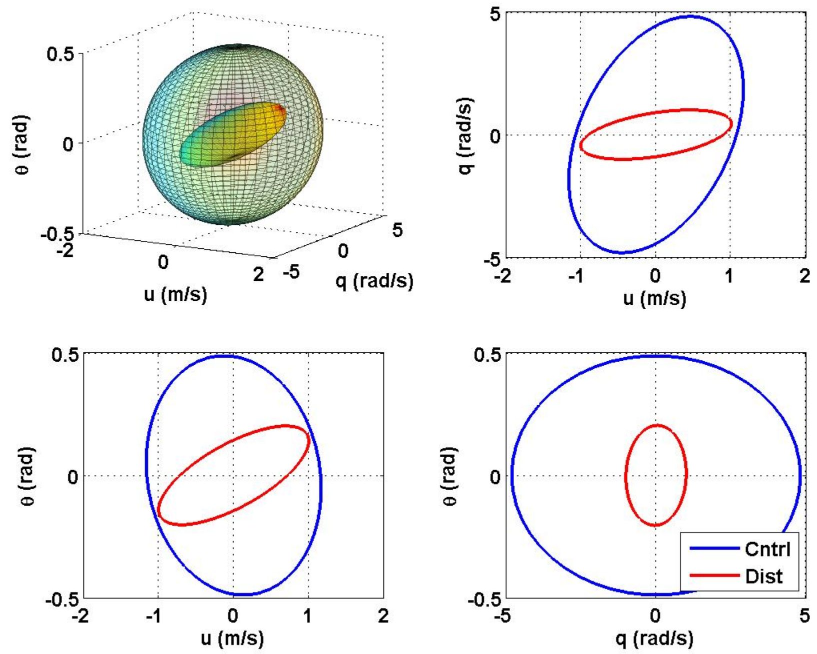

Figure 4.5: Controllability Ellipsoid Bounding the Disturbance Ellipsoid

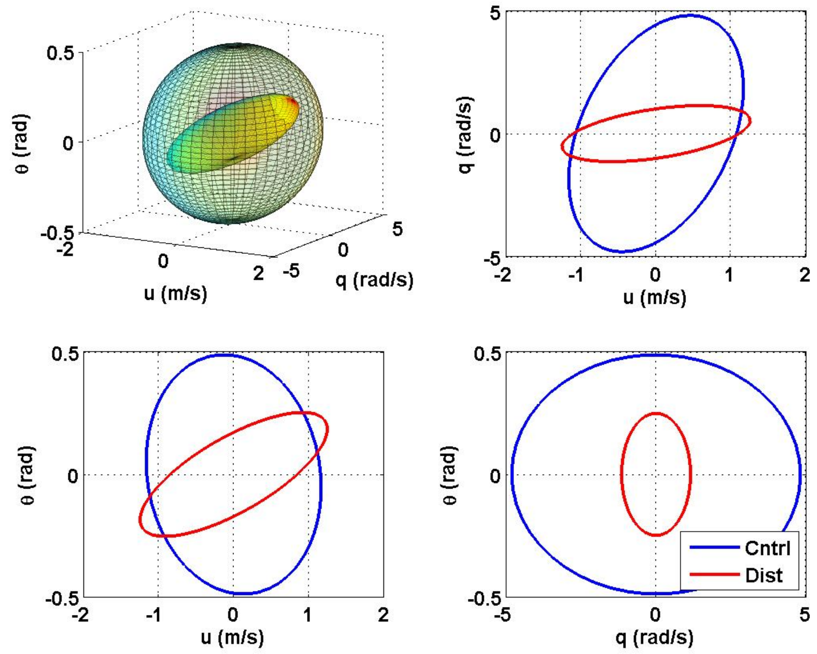

Figure 4.6: Unbounded Disturbance Ellipsoid

To prove these predictions, the out-loop needs to be formulated and closed. The outer states are $\vec{x} = [u, q, \theta, x]^T$, where the x position is determined by integrating the u velocity. The state space model is shown in 4.20, where the upper left 3x3 submatrix of $\mathbf{A}_O$ is $\mathbf{A}_{CL}$. Zeros are added to $\mathbf{B}$ and $\mathbf{G}$ to account for the added state as seen in Equations 4.20. The Vicon$^{\text{TM}}$ system measures position, x, and u velocity and is reflected in 4.20.

$$\begin{gathered}
\mathbf{A}_O = \begin{bmatrix} -0.4425 & 0.0169 & -9.2773 & 0 \\ 19.5699 & -14.5999 & -92.5917 & 0 \\ 0 & 1.0000 & 0 & 0 \\ 1.0000 & 0 & 0 & 0 \end{bmatrix} \qquad \mathbf{B}_O = \begin{bmatrix} 0 \\ 0.6944 \\ 0 \\ 0 \end{bmatrix} \\
\mathbf{D}_O = \begin{bmatrix} 0.4703 & 0.6005 \\ 0 & 17.3849 \\ 0 & 0 \\ 0 & 0 \end{bmatrix} \qquad \mathbf{C}_O = \begin{bmatrix} 0 & 0 & 0 & 1 \\ 1 & 0 & 0 & 0 \end{bmatrix}
\end{gathered} \tag{4.20}$$

Once the outer-loop matrices are formed, the static $\mathcal{H}_\infty$ procedure outlined in §4.3 is used to develop a static controller. The weighting matrices for this process are found in 4.21, with $\gamma = 50$ and the resulting static gains are given in 4.22. Now, the system has been formulated, a simulation can be performed to confirm the intuition stated earlier. The Simulink$^{\text{TM}}$ feature developed by Matlab$^{\text{TM}}$ will simulate the feedback control for the microquad model under the given conditions. The basic structure of the Simulink$^{\text{TM}}$ model is shown in 4.7. A saturation block is used to constrain the maximum control input allowed.

$$\mathbf{Q} = \begin{bmatrix} 10 & 0 & 0 & 0 \\ 0 & 10 & 0 & 0 \\ 0 & 0 & 1 & 0 \\ 0 & 0 & 0 & 10000 \end{bmatrix} \qquad \mathbf{R} = \begin{bmatrix} 1 \end{bmatrix} \tag{4.21}$$

$$\mathbf{K} = \begin{bmatrix} -105.3855 & -40.7541 \end{bmatrix} \tag{4.22}$$

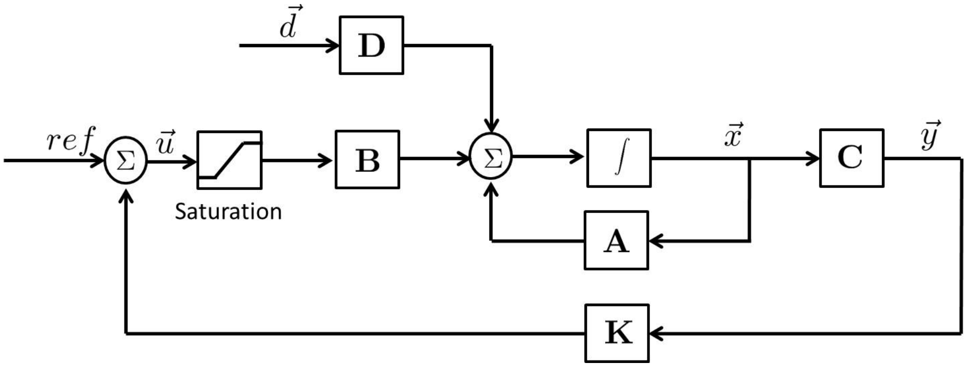

Figure 4.7: Motor Response to a Chirp Input

The simulation results from the two scenarios are shown below. First, examine the results from case one with a constant disturbance input of $\vec{d}_{max} = [d_{u,max} d_{q,max}] = [4\ m/s, -0.2\ rads/s]^T$, represented in 4.8. From the gramian base analysis it was predicted that the vehicle had adequate control authority to reject this disturbance. It is seen that all states come to a steady state value and the vehicle is able to hold its position. The control input is below the saturation level. The microquad is adequately able to reject this given disturbance. For the second case, a constant disturbance of $\vec{d}_{max} = [5\ m/s, -0.2\ rads/s]^T$ is applied. The gramian analysis predicts that the vehicle would fail to reject such a disturbance. Figure 4.9 clearly shows that the vehicle does not have the proper control authority to attenuate this disturbance condition. The u-velocity never returns to zero, which results in the vehicle drifting away from the reference position as indicated with the x-position. The longitudinal control input saturates as expected, since the vehicle is unable to reject the disturbance. A stabilizing outer-loop controller does not affect whether the vehicle will properly reject a disturbance; however, it does affect the performance of the vehicle such as rise time, over shoot, and steady state error, to name a few.

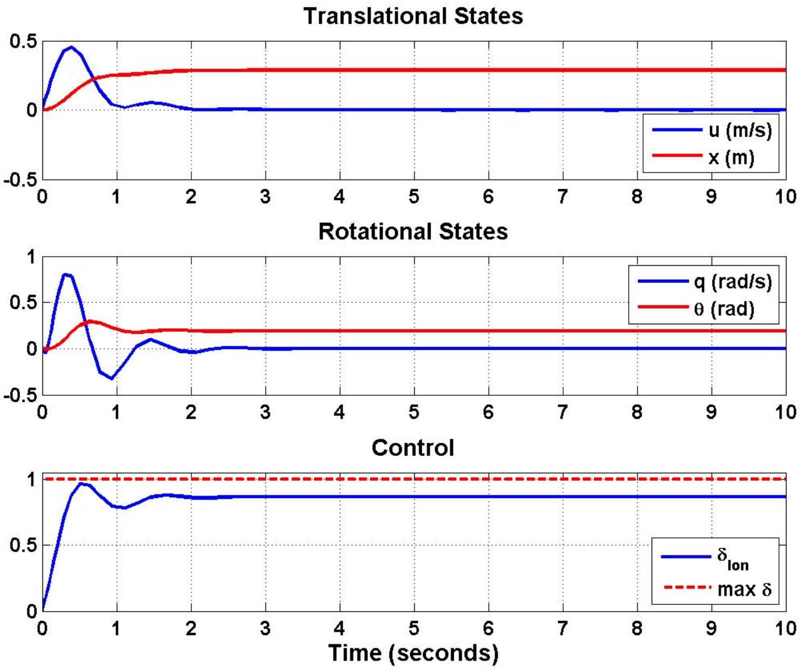

Figure 4.8: Simulation Results with a Bounded Disturbance Ellipsoid

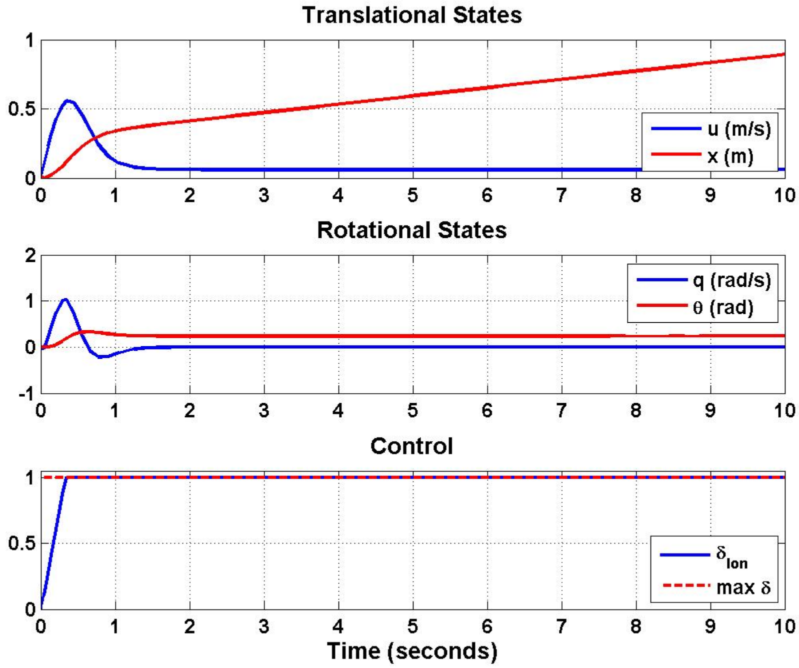

Figure 4.9: Simulation Results with an Unbounded Disturbance Ellipsoid

This example demonstrates several useful facts. This provides a means to determine the maximum disturbance a vehicle can reject with a specified limit on control. This method is not limited to single direction disturbances, but can look at combinations of disturbances, as can be seen in the previous example, where both d_u and d_q were considered. In this case, it was useful to only explore a 3 state stable inner-loop system to help visualize this approach, but it can also be expanded to larger systems, by partitioning the SVD matrices by the states of interest.

There are a couple of notes about this method that should be clearly stated. The gramian ellipsoid analysis does not provide a limit to the upper bound of a disturbance that a vehicle can reject, instead it only guarantees the vehicle is able to reject that disturbance. It has been found that for this specific situation the most important bounded disturbance gramian 2-D projection deals with rates, i.e. for longitudinal dynamics, u and q must be bounded for the vehicle to reject the disturbance, meaning the disturbance ellipsoid is not bounded in the θ state. It is possible that it is important to bound if, for instance, the vehicle was performing a maneuver that requires tracking a specific attitude. It has also been observed that different outer-loop feedback controllers allow the vehicle to reject different magnitudes of disturbances; however, each controller design will still be able to reject the disturbance indicated by this gramian based method. In this case, the closed inner loop, $\mathbf{A}_{CL}$, matrix was used. This was necessary, because the microquad itself is inherently unstable. Once a stable inner-loop was formulated, this method was employed to obtain information regarding the outer-loop station keeping.

The example above used less than optimal weighting matrices to illustrate the effectiveness of this method. Now, let's return to the controller design that was outlined in §4.4. The gramian base method will be preformed on the closed inner system, and the simulations will be carried out with the outer loop control scheme constructed in §4.5. Each individual disturbance will be evaluated separately to provide a maximum magnitude the vehicle can reject for that given disturbance.

Since, the model developed for the microquad is decoupled, which will be reaffirmed with the analysis performed in §4.9, it is convenient to partition the matrices into longitudinal, lateral, heave and yaw categories. First, the longitudinal direction will be explored, and the closed inner-loop matrix will be partitioned to include the $\vec{x} = [u, q, \theta]^T$ states, the $\vec{u} = [\delta_{lon}]$ control, and the $\vec{d} = [d_u, d_q]^T$ disturbances. The control input will be scaled by the value of 35, which bounds the control input. With these parameters in place, the reachability ellipsoid is found. For a d_u disturbance it was determined that the vehicle can reject a $4m/s$ gust. The resulting ellipsoids found by the gramian analysis is illustrated in Figure 4.10, and the simulation confirming the rejection of a $4m/s$ disturbance is shown in Figure 4.10. Next, the rotation component, d_q was examined. A disturbance input of $d_q = 1.27rad/s$ is used to scale the disturbance matrix. The reachability and disturbance ellipsoids are depicted in Figure 4.12. The resulting simulation verifying the results are given in Figure 4.13.

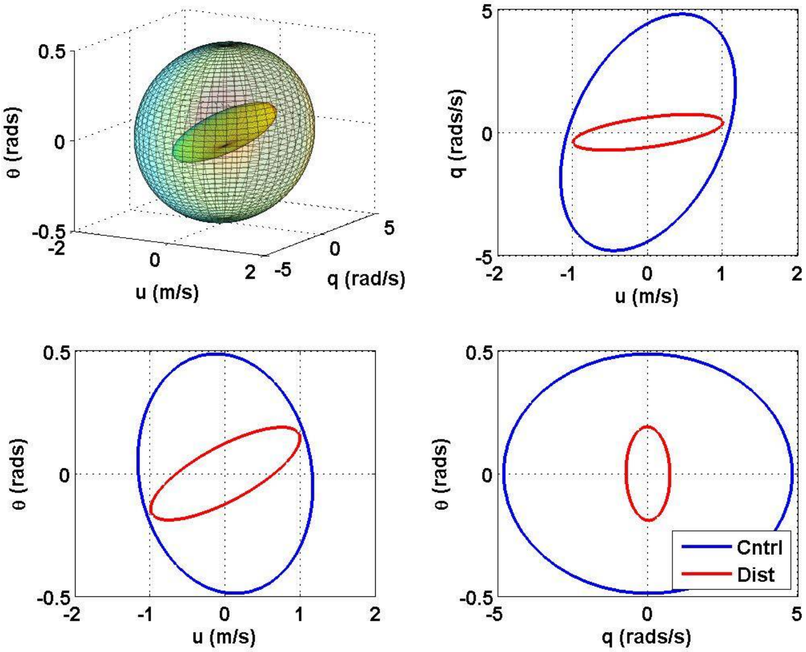

Figure 4.10: Gramian Ellipsoid for $d_u = 4m/s$ Disturbance

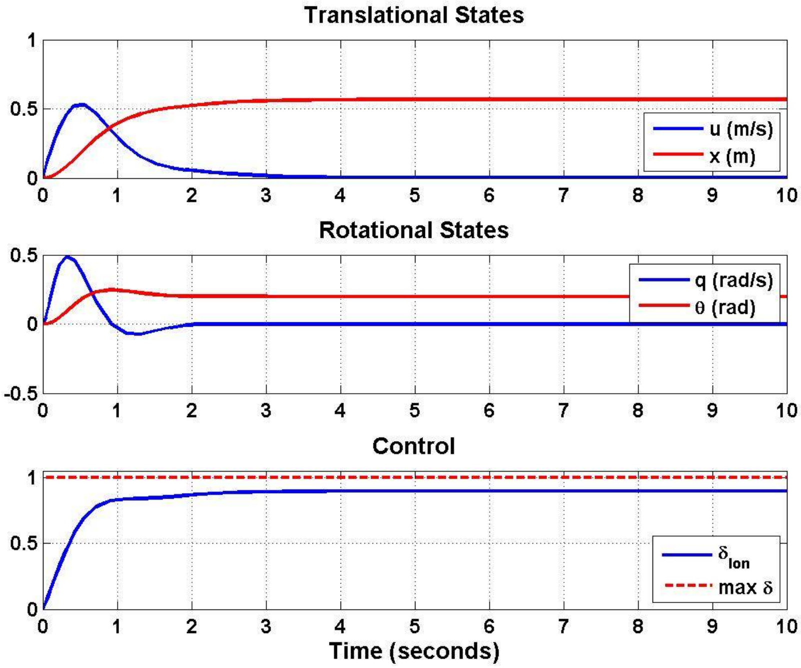

Figure 4.11: Simulation Verification for $d_u = 4m/s$ Disturbance

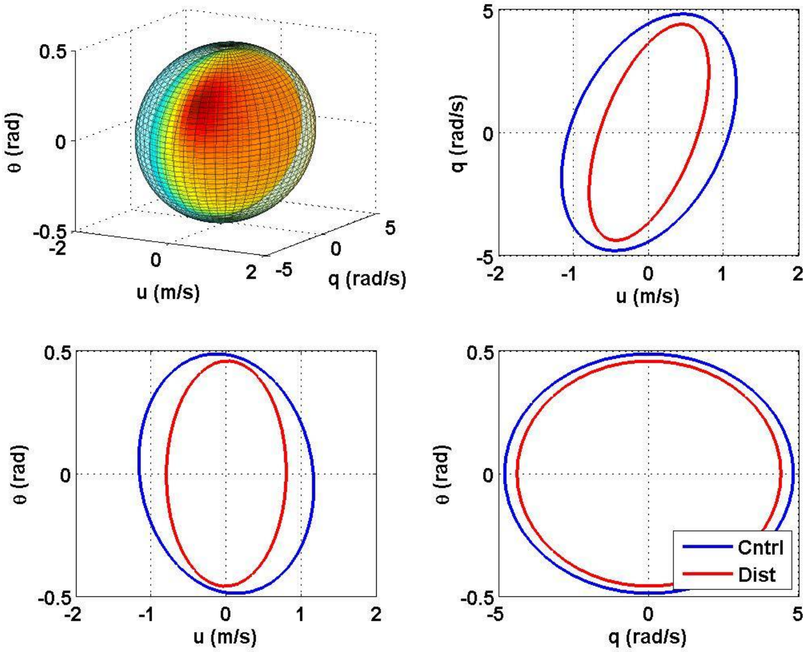

Figure 4.12: Gramian Ellipsoid for $d_q = 1.27 rad/s$ Disturbance

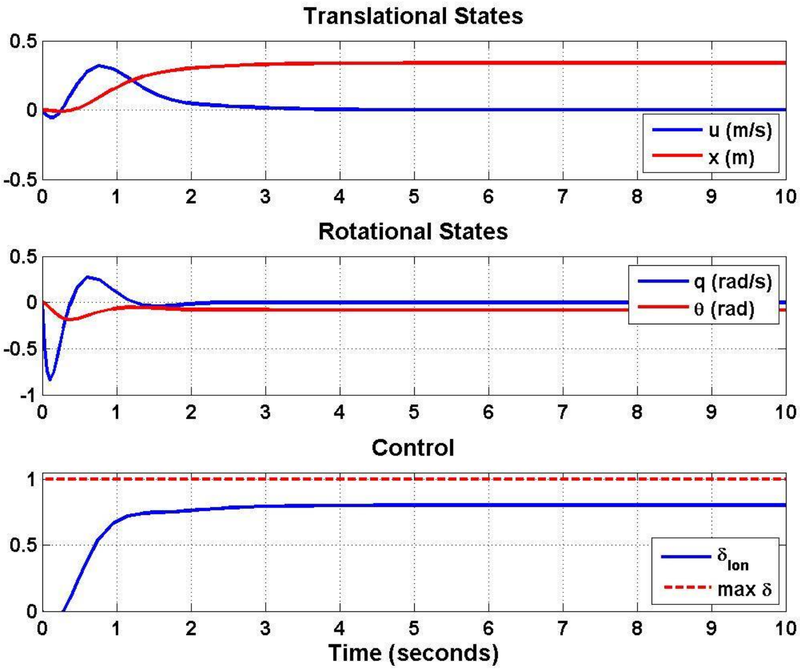

Figure 4.13: Simulation Verification for $d_q = 1.27 rad/s$ Disturbance

Next, the lateral dynamics are considered. Here, the closed inner-loop system was partitioned to include $\vec{x} = [v, p, \phi]^T$ states, $\vec{u} = [\delta_{lat}]^T$ input and $d = [d_v, d_p]^T$ disturbances. Again, the maximum control allotted for disturbance rejection is 35 control units, so the control matrix was multiplied by this value to scale the control input to 1. It is found that the vehicle can reject a $d_v = 6.1 m/s$ and a $d_p = 1 rad/s$ disturbance independently. The respected analysis and simulations are shown in Figures 4.14, 4.15, 4.16, and 4.17.

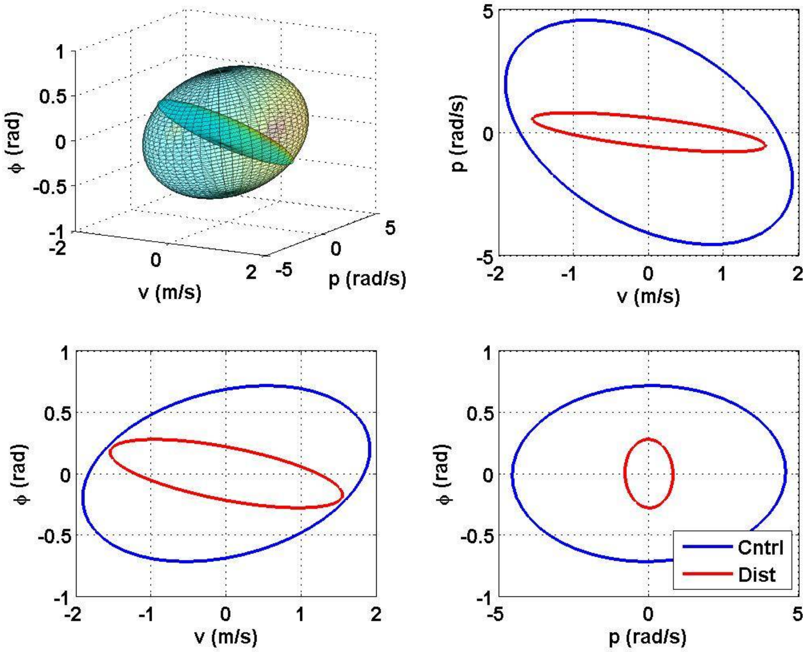

Figure 4.14: Gramian Ellipsoid for $d_v = 6.1 m/s$ Disturbance

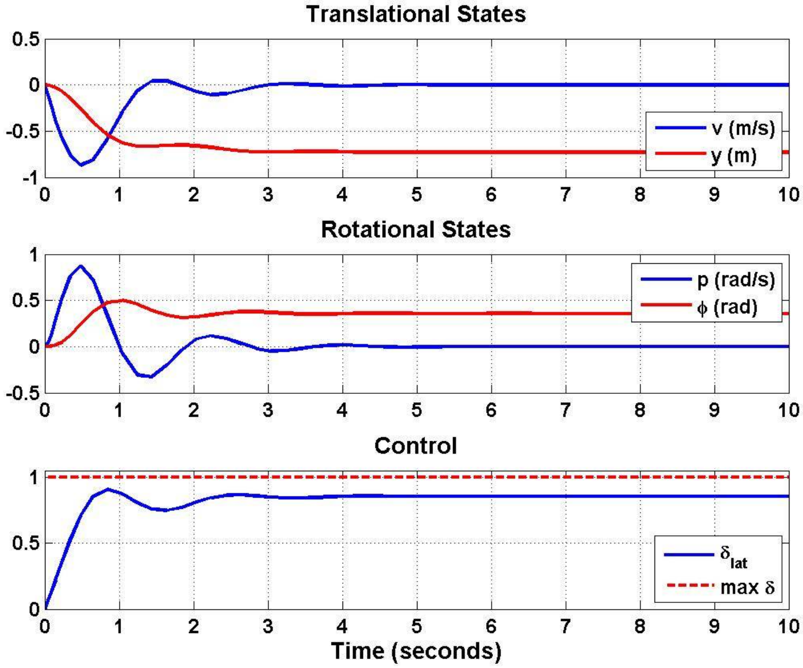

Figure 4.15: Simulation Verification for $d_v = 6.1 m/s$ Disturbance

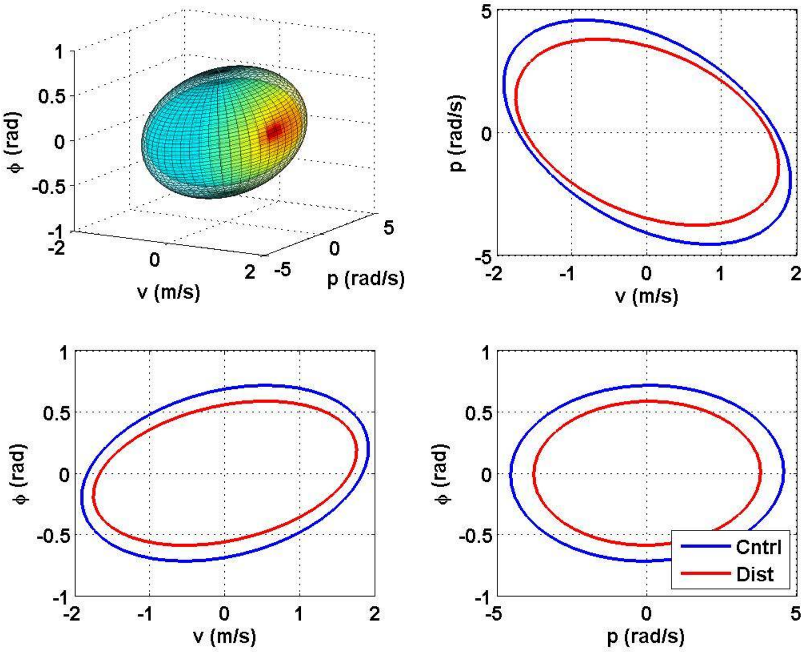

Figure 4.16: Gramian Ellipsoid for $d_p = 1 rad/s$ Disturbance

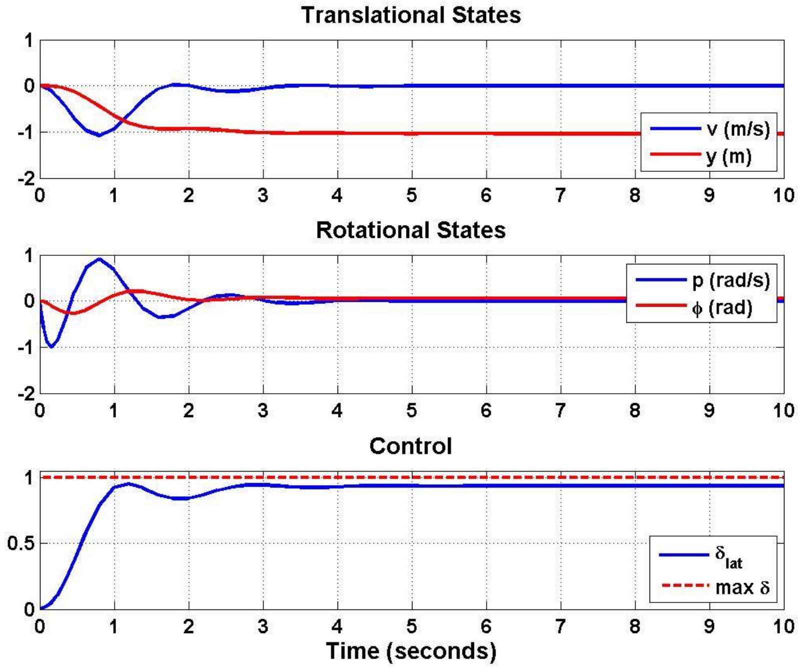

Figure 4.17: Simulation Verification for $d_p = 1 rad/s$ Disturbance

For heave and yaw dynamics, the analysis is greatly simplified, due to having one state for the inner-loop. For the disturbance gramian to be contained in the reachability gramian the simple relationship needs to be satisfied 4.23, since the control and disturbance only act in a single direction. The vehicle has poor control authority in the heave direction, which is reinforced in §4.10. For this reason, the control matrix is multiplied by 70 control units. The maximum d_w disturbance the vehicle is able to reject is $1.75 m/s$. The resulting simulation to verify this is found in Figure 4.18. The yaw dynamics take a much smaller amount of control energy to reject a d_r, which will be reflected in §4.10. Due to this, the yaw control matrix was scaled to 1 with the maximum control input of 10 units. Using the relation in 4.23, the microquad can reject a $d_r = 1.8 rad/s$ disturbance. The simulation verifying these findings is shown in Figure 4.19. A table summarizing the findings of this section are listed in Table 4.1.

$$X_c^{\frac{1}{2}} \geq X_d^{\frac{1}{2}} \tag{4.23}$$

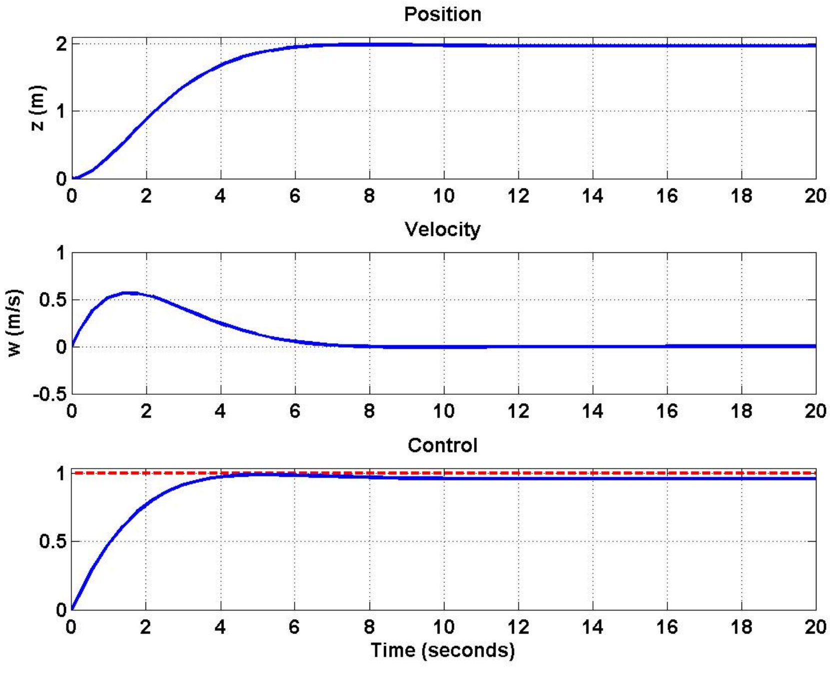

Figure 4.18: Gramian Ellipsoid for $d_w = 1.75m/s$ Disturbance and Simulation Verification

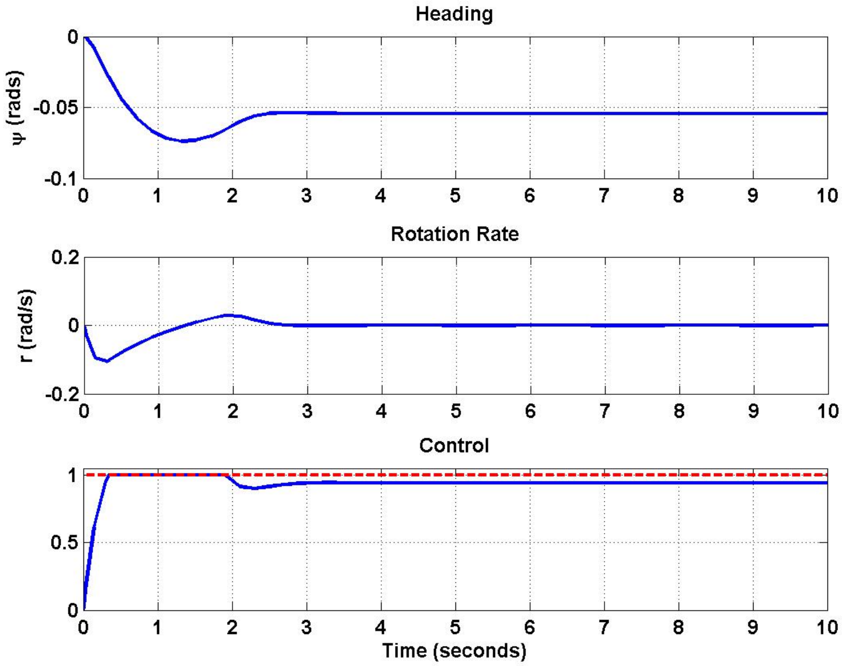

Figure 4.19: Gramian Ellipsoid for $d_r = 1.8 rad/s$ Disturbance and Simulation Verification

Control	Input	Disturbance Parameter	abs Max
δ_{lon}	35	d_u	4 m/s
δ_{lon}	35	d_q	1.27 rad/s
δ_{lat}	35	d_v	6.1 m/s
δ_{lat}	35	d_p	1 rad/s
δ_{thr}	70	d_w	1.75 m/s
δ_{yaw}	10	d_r	1.8 rad/s

Table 4.1: Max Disturbance by Bounded Control Input

4.8 $M_{u,g}$ Sensitivity Study

To explore the non-linear loading observed from a u velocity disturbance in torque about the y-body axis, three alternate scenarios will be explored here using the longitudinal model. Figure 4.20 shows a closer look the non-linear loading due to the u velocity component, but this can be broken down to two distinct linear trends. Each linear curve fit yields a disturbance derivative. Initially, this non-linear trend was attributed to the vehicle flexing and twisting in the test apparatus, but will be consider here to explore the effect of the gramian analysis as the disturbance changes. The resulting disturbance derivatives are $M_{u,g} = 27.44$ and $M_{u,g} = -12.27$. The third scenario will be the negative of the M_u stability derivative. Table 4.2 sums up the results from the gramian method. From the table, there is a drastic effect when including this term. All three scenarios results in about 1 m/s disturbance rejection, while when this term was not included, it was determined to be 4 m/s.

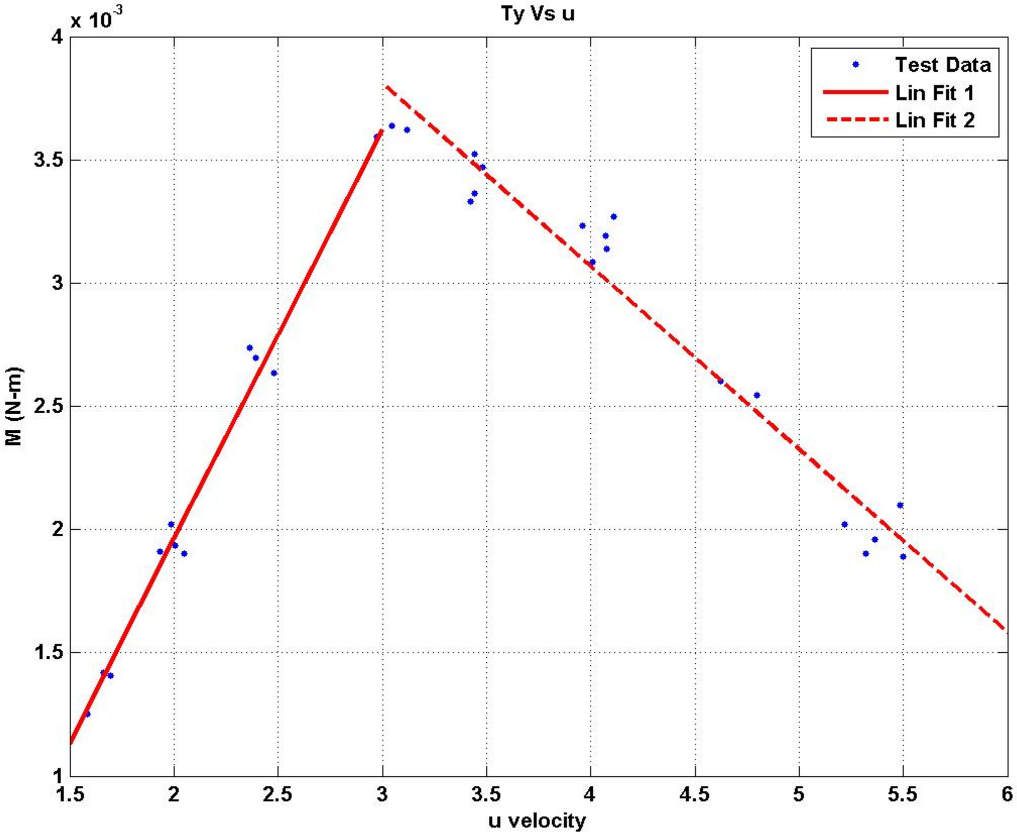

Figure 4.20: Vehicle Ty Loading Due to u Velocity Component

$M_{u,g}$	Resulting d_u (m/s)
27.44	0.84
-12.27	1.3
19.57	1.15

Table 4.2: Gramian Results from three $M_{u,g}$ Scenarios

Next, $M_{u,g}$ was arbitrary changed through a range of -20 to 20 to see the effects on the gramian analysis. Figure 4.21 shows the results of this procedure. This graph demonstrates the importance of having an accurate model, as there is a large difference in the results as the disturbance derivative changes.

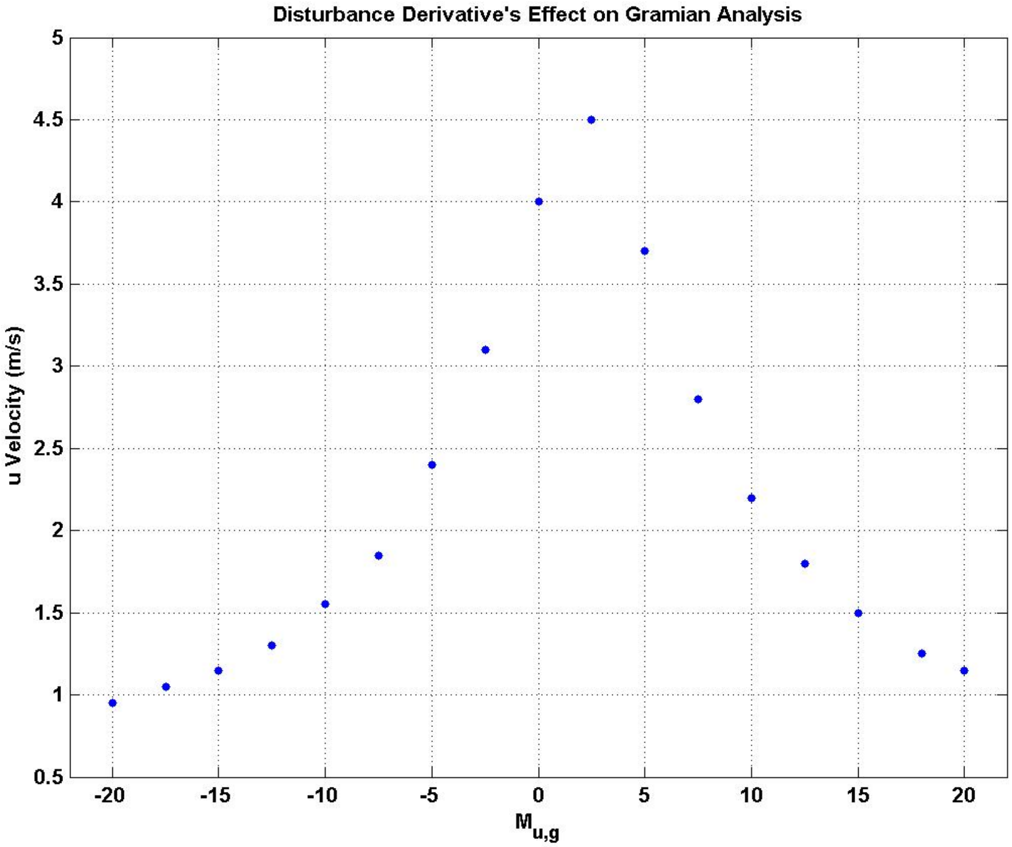

Figure 4.21: Progression of gramian method on u velocity as $M_{u,g}$ varies

4.9 Disturbance and Control Direction Analysis

This section will explore the directionality of the plant and provide a measure for the direction of each distance. This analysis is important, as it provides a measure on which disturbances affect the plant the most. This measure is referred to as the plants 'resilience'. The concept is to assume the plant has perfect control, as described in [22], [20]. In this case only the disturbance is being considered, so perfect control can be thought of as $u = -G^{-1}G_d d$, meaning the control inputs mirror the disturbance inputs. Thus, this evaluation provides insight into the inherent control properties of the plant and indicates 'good' and 'bad' control directions. In other words, if the plant has perfect control and the plant still has poor control for the given disturbance, then the response of the plant will be poor no matter which controller is implemented – assuming perfect control indicates directional strengths and weaknesses of the plant.

For this analysis, we will consider an LTI system with a transfer function matrices (TFM) as shown in 4.24, where $G(s)$ is the TFM of the plant, $u(s)$ is the control input, $G_d(s)$ is the TFM for the disturbances, and $d(s)$ is the disturbance input.

$$y(s) = G(s)u(s) + G_d(s)d(s) \tag{4.24}$$

Here, $G(s)$ is a 4x4 matrix with measurements of $\vec{y} = [u, v, w, r]^T$, which are ultimately the steady state measurements with the inputs of $\vec{u} = [\delta_{lon}, \delta_{lat}, \delta yaw, \delta thr]^T$, while the disturbance TFM, $G_d(s)$, has inputs of $\vec{d} = [d_u, d_v, d_w, d_p, d_q, d_r]^T$. It is important in this analysis to scale the control and disturbance inputs by the maximum expected disturbance and control. The results from Table 4.1 are used to scale the respected **B** and **D** matrices. The transfer function matrix is easily computed from the state space mode with Equation 4.25, where **C** will give measurements of $[u, v, w, r]^T$. Similarly, $G_d(s)$ is calculated by Equation 4.26.

$$\mathbf{G(s)} = \mathbf{C}(s\mathbf{I} - \mathbf{A})^{-1}\mathbf{B} \tag{4.25}$$

$$\mathbf{G_d(s)} = \mathbf{C}(s\mathbf{I} - \mathbf{A})^{-1}\mathbf{D} \tag{4.26}$$

Once the plant and disturbance TFM are calculated, it is easiest to work with the steady state gain TFM. This is calculated by $\lim_{s\to 0} G(s)$ or is found by using Matlab$^{\text{TM}}$'s 'dcgain' command. The resulting steady state gain matrices are found in 4.27 and 4.28.

$$\mathbf{G(s)} = \begin{bmatrix} -0.9787 & 0 & 0 & 0 \\ 0 & 1.2868 & 0 & 0 \\ 0 & 0 & 0 & -1.8934 \\ 0 & 0 & 0.4029 & 0 \end{bmatrix} \tag{4.27}$$

$$\mathbf{G_d(s)} = \begin{bmatrix} 0.9013 & 0 & 0 & 0 & -0.4948 & 0 \\ 0 & 1.6770 & 0 & 1.3341 & 0 & 0 \\ 0 & 0 & 1.8201 & 0 & 0 & 0 \\ 0 & 0 & 0 & 0 & 0 & 0.1084 \end{bmatrix} \tag{4.28}$$

The first step in this process is to calculate the Relative Gain Array (RGA), shown in Equation 4.29, where the symbol × is element by element multiplication [20]. For the microquad, the results are trivial and seen in 4.30. This means the microquad model is decoupled and a longitudinal input will only excite a longitudinal output. This reaffirms the approach taken in § 4.7 of partitioning the system into longitudinal, lateral, heave and yaw dynamics.

$$RGA(G) = \Lambda(G) = G \times (G^{-1})^T \tag{4.29}$$

$$\Lambda(G) = \begin{bmatrix} 1 & 0 & 0 & 0 \\ 0 & 1 & 0 & 0 \\ 0 & 0 & 0 & 1 \\ 0 & 0 & 1 & 0 \end{bmatrix} \tag{4.30}$$

Next the condition number, γ, is calculated by the ratio between the maximum and minimum singular value as shown in Equation 4.31. This value is largely dependent on how the matrices are scaled. This provides a measure of the input-output controllability of the plant. Using Equation 4.31, yields a condition number of $\gamma(G) = 10.9635$.

$$\gamma(G) = \overline{\sigma}(G)/\underline{\sigma}(G) \tag{4.31}$$

Finally, the disturbance condition number is computed. This provides a measure for how each disturbance is aligned with the plant and is calculated by Equation 4.32, where d denotes each disturbance. A smaller number indicates the disturbance is in a 'good' direction and is aligned with the plant, and a larger number is a 'bad' direction and the disturbance is more difficult to reject. The disturbance condition number is bounded between 1 and the condition number. This expression is shown in 4.33 from [24].

$$\gamma_d(G) = \frac{||G^{-1}d||_2}{||d||_2}\bar{\sigma}(G) \tag{4.32}$$

$$1 \leq \gamma_d(G) \leq \gamma(G) \tag{4.33}$$

The results from the disturbance condition number are shown in Table 4.3. For a vertical disturbance, w is best aligned with the plant, which is logical, considering all four motors directly act in the z_b direction. The actuation can directly match the disturbance. The longitudinal and lateral cases have slightly larger disturbance condition number. This is due to the actuators not directly causing a u or v velocity. The actuators for these directions change the attitude of the vehicle, which leads to a translational velocity. The vehicle is easiest perturbed in heading. This is also a logical result because this pole is closest to the origin, meaning that it is near neutrally stable [15]. This means the yaw mode is easily perturbed, but from the results of the gramian analysis, it is known that the microquad has larger control authority in the yaw direction.

	d_u	d_v	d_w	d_p	d_q	d_r
$\gamma_d(G)$	1.9346	1.4714	1.0000	1.4714	1.9346	10.9635

Table 4.3: Disturbance Condition Number

4.10 Control Energy Analysis

This section focuses on control energy. Typically, atmospheric disturbances are modeled with a shaping filter with a white noise input [10]. The dynamics of this filter are normally embedded into the **A** for analysis purposes. However, this causes the solution to the Lyapunov Equation to be singular and not invertible due to the inability to control the disturbance states. Therefore, for this analysis, the model will be left unaltered from 3.9, but will assume a white noise input for the disturbances. Kang et al [25], proposes a means of measuring the control energy of a system with a white noise input. The framework to the problem requires a LTI model in the form 4.34, with a Gaussian white noise input for the disturbance. Here S_w is a matrix with intensities of the disturbance input and is defined to have zero mean and a known correlation function as seen in Equation 4.35.

$$\dot{\vec{x}} = \mathbf{A}\vec{x} + \mathbf{B}\vec{u} + \mathbf{D}\vec{d} \tag{4.34}$$

$$R_d(\tau) = E[d(t)d^T(t+\tau)] = S_w\delta(\tau) \tag{4.35}$$

Then, a disturbance sensitivity gramian is formulated [25] and solved using the following Lyapunov Equation 4.36. Using this coupled with the results from the controllability gramian 4.14 a Disturbance control measure, ρ, is determined with Equation 4.37, where the over bar denotes steady state.

$$AX_d + X_dA^* + DS_wD^* = 0 \tag{4.36}$$

$$\rho = \int_0^\infty \mathbf{E}[u^T(t)u(t)]\mathrm{d}t = trace\{\bar{X}_c^{-1}\bar{X}_d\} \tag{4.37}$$

Using the analysis method above, the energy to control each separate disturbance is examined. This measure of control energy is unit-less, but will provide insight on which disturbances will require the most energy for rejection. For simplicity, 1 will be used for the noise intensity for the disturbance input. The results of this analysis are reflected in Table 4.4. Let's examine the translational, $\vec{d} = [d_u, d_v, d_w]^T$, disturbances first. Since the microquad is fairly symmetric, the control energy to reject the u and v disturbance is about the same. A d_w disturbance takes about 13 times more energy to reject a disturbance in that direction. It should be noted that the previous method determined how well a disturbance aligned with the plant, while this method focuses on the amount of control energy required to reject a given disturbance. Although the d_w disturbance requires a large amount of control energy, the microquad at least is well aligned with the disturbance. This result is also reflected in the gramian based analysis, in which it took double the control input to reject a third of the disturbance input. The disturbance rotation components, $\vec{d} = [d_p, d_q, d_r]^T$ have a similar trend where the longitudinal and lateral disturbances are roughly the same magnitudes. Again, it is contributed to a symmetric airframe. The d_r disturbance takes little control energy to reject the disturbance. This also aligns with the results from the gramian analysis. The yaw dynamics are nearly neutrally stable; although it is easily perturbed from its trim flight condition of hover, yaw perturbations take little control energy to return the vehicle to a trim condition. This is also ideal, as the directional analysis determined this disturbance was least aligned with the plant of the microquad.

	d_u	d_v	d_w	d_p	d_q	d_r
ρ	1.5123	1.4704	19.3119	1.5333	1.3040	0.0223

Table 4.4: Relative Energy Measure

4.11 Actuator Bandwidth

Bandwidth is an important measure, as it illustrates which frequencies the vehicle is able to operate effectively. Using the model response model found in §3.3.9, the control bandwidth is easily determined. Bandwidth has multiple definitions, but is typically defined when the magnitude of the response falls by 3 dB from its low frequency value [10]. This is denoted in Figure 4.22. The motors have a bandwidth of $\omega_B = 3.6Hz$. The actuator bandwidth is at the low end for actuator response of a vehicle at this size. From open loop flight data, shows the vehicle body dynamics are $\tilde{4}$ Hz, so this control bandwidth is nearly inadequate. Figure 3.21 showed the motors had good coherence just above 10 Hz. This suggests that smaller amplitude control actuation may have high bandwidth. Still, this is short of the ideal control bandwidth Pisano [3] calculated, which is in the range of 10 Hz to 15 Hz. Clearly, this is a limitation for the vehicle in controlling both the body dynamics and the disturbance rejection. Bandwidth provides the frequency at which roll off occurs. This means as frequency increases the actuators become less effective.

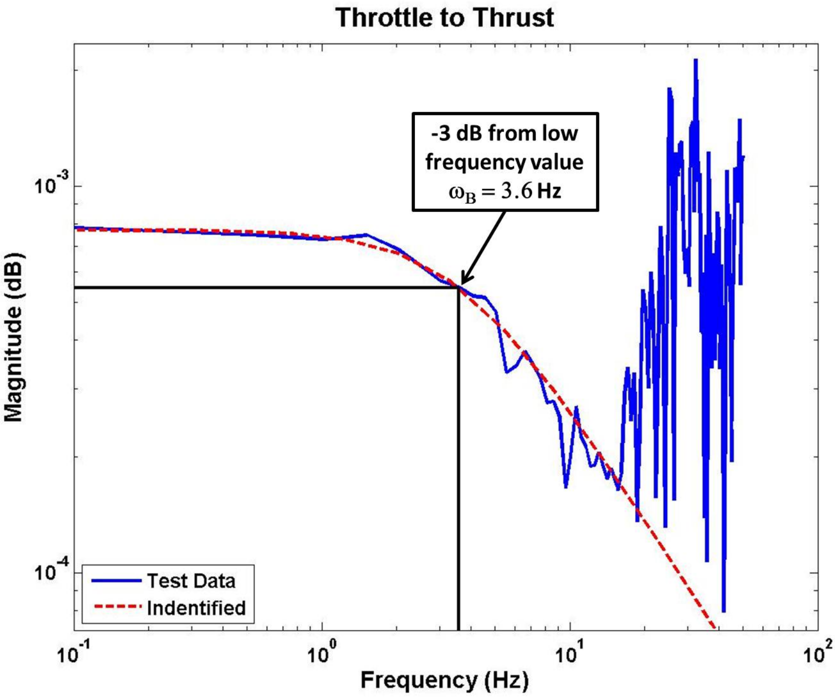

Figure 4.22: Control Bandwidth from the Spectral Analysis of the Motor Response

Power Density Spectrum (PSD) is typically used to describe gust disturbances. This represents the mean squared value of a stochastic process. The PSD from the disturbance generator is determined by collecting velocity data. For the PSD, data was sampled at 100 Hz for 500 seconds. Using the 'periodogram' function in Matlab$^{\text{TM}}$ provides the power distribution of the disturbance at each frequency. Figure 4.23 shows the PSD from the disturbance generator. The gust generator had a constant operating condition; this is clearly seen as the magnitude rolls off at a low frequency. This is the typical shape of a PSD and is often represented with a shaping filtering. Common shaping filters used to model this behavior are the von Karman and Dryden. Here, a Dryden shaping filter was fit to the data, as can be seen by the dashed red line. Equation 4.38 is the general formulation for the Dryden model [26]. The disturbance generator PSD shows good agreement with the shape of the classic Dryden model.

$$\Phi(\Omega) = \sigma_w^2 \frac{2L}{\pi} \frac{1 + 3L^2\Omega^2}{[1 + L^2\Omega^2]^2} \tag{4.38}$$

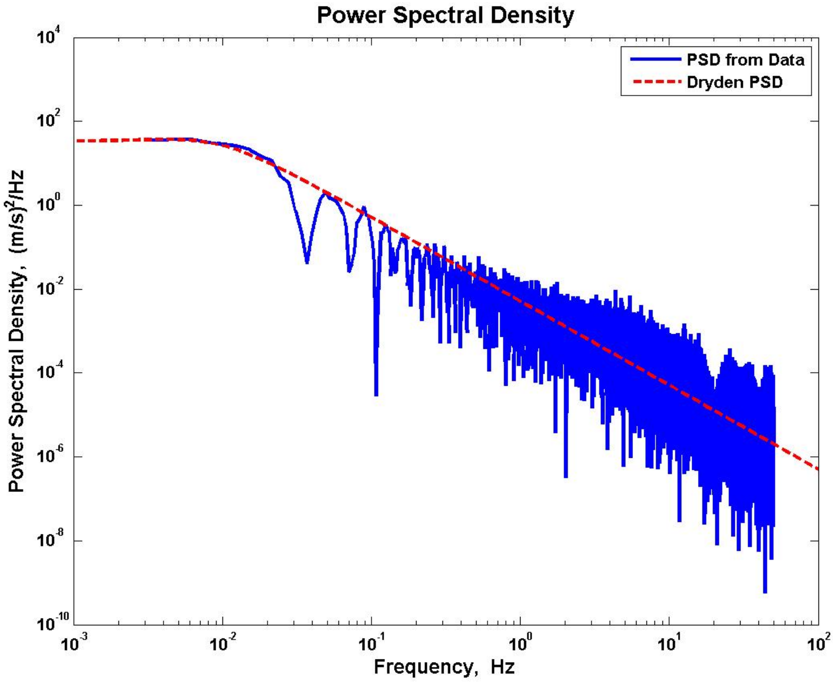

Figure 4.23: PSD from Gust Generator
s

The microquad has adequate control bandwidth to control the vehicle in the disturbance conditions the gust generator can produce. Clearly, the frequency content of the disturbance falls off at a lower frequency than the actuators. This suggests that the vehicle has the control authority to reject this disturbance. However, the microquad will have difficulties if the disturbance has a greater spatial content, which will push the roll off point to a higher frequency. Once the Control bandwidth is eclipsed, the microquad will have more difficulties rejecting such disturbances. Bandwidth is a vital measure when determining if a vehicle can successfully reject gust disturbances.

Chapter 5

Conclusion

The goal of this dissertation is to explore the disturbance rejection properties of the microquad and to provide a framework analysis method that can be applied to any vehicle at this scale. Micro Air Vehicles have a large range of platform configurations and a number of envisioned missions. Therefore, it is crucial to provide a disturbance rejection analysis for trade studies that are being performed for vehicle selection. This type of analysis is vital for determining whether a vehicle is able to carry out a mission. These small vehicles are vulnerable to disturbances, and this framework provides a means for comparing vehicle configurations. For an effective assessment of a vehicle, it is important to attain an accurate LTI model. This work utilizes the LTI model identified by Miller [15], and builds upon this model with a bench-top tests. The test data from the experiment yield disturbance derivatives about hover. Through this combination, the effectiveness of disturbances on the microquad is evaluated. Once an accurate model is achieved, a full analysis process can be carried out. The list below provides a summary of accomplishments:

- Successfully identified the disturbance matrix for the microquad, which is vital for control design, simulations and analysis purposes.

- Presented the framework for a measure to determine disturbance magnitude bounds. This is achieved by creating reachability and disturbance ellipsoids defined by the singular value decomposition of their respected gramian. These findings were then verified through simulations.

- Explored the directionality of the disturbance using a procedure that assumed perfect control, and thereby attained findings that related disturbance parameters to the direction of the plant dynamics of the microquad. This provides insight into which disturbance parameters the vehicle is most susceptible to, independent of the control scheme.

- Analyzed relative control energy required for each disturbance parameter. This gave insight into the effectiveness of actuators in order to attenuate a disturbance.
- Motor dynamics were identified, which yielded the actuator bandwidth for the microquad. This result was compared to the Power Density Spectra generated by the fan bank system.

5.1 Concluding Remarks

As stated earlier, the microquad is an inherently unstable platform that requires both an inner and outer-loop control strategy. The analysis tools explored provide a means to measure disturbance properties independent of control; however, since the microquad requires a stabilizing inner-loop, the analysis process starts from this baseline. This is reasonable, as Miller [15] did not see a drastic performance difference between different control strategies for the inner-loop. Most of the vehicles at this scale will require a stabilizing inner-loop control since highly maneuverable platforms are inclined to be unstable. Once this baseline inner-loop is attained, the vehicle's disturbance rejection characteristics are examined independent of outer-loop control. This is important, as different control designs can skew the performance of the plant under different disturbance conditions.

This disturbance analysis examines three different areas. The first method uses a gramian based approach with a bound on the control input. Once this limit is determined, the maximum disturbance the vehicle can reject is found independent of control strategy for the outer-loop. This is a great measure that determines the maximum disturbance the vehicle is able to reject with feedback control. The reverse problem could easily be explored, by examining how much control input is required to attenuate a given disturbance. The second method explores how aligned a disturbance is with plant dynamics. This provides a measure to see which disturbances are easiest to reject and which ones the vehicle are most vulnerable to. The final method examined the amount of control energy required to reject a given disturbance. In this instance, the translational and rotation components were considered separately. This compliments the second analysis method nicely. Although a disturbance may align with the plant, it could still take a large amount of control effort to reject a disturbance.

This process revealed what intuition suggests about the quadrotor. For example, the direction study showed that the vehicle is best aligned to reject a vertical disturbance. This is obvious, due to all four actuators providing direct control in that direction. However, the amount of control energy required is far greater than the other translational disturbance. This is due to the vehicle having to produce the thrust to overcome the disturbance, while the longitudinal and lateral directions only need a small differential in thrust to create a moment to change the vehicle attitude. Both longitudinal and lateral components were rather similar, which is expected, as the vehicle is fairly symmetrical about the x- and y-body axes. The yaw dynamics is easily perturbed from trim, meaning it is not well-aligned with the plant. This is due to the pole being close to the imaginary axis, causing the vehicle to be near neutrally stable. However, the energy analysis shows that it takes little control energy to reject a disturbance.

All of these findings are also reflected in the gramian based analysis. The longitudinal and lateral dynamics yielded similar results with the amount of disturbance the vehicle can attenuated with a specified control bound. This method showed that the microquad required larger control authority to reject a smaller gust input for a vertical disturbance then the other translational states. Finally, the yaw state required a smaller input to reject a rotational gust then its longitudinal and lateral counterparts. These three techniques support each other's findings, and provide knowledge on which components the microquad can easily reject, as well as give an upper limit on the magnitude of the disturbance the microquad can reject for bounded control input.

Finally, the results from these procedures are all based on a linear model about hover. This model is a small perturbation model; therefore this analysis process has its limitations. However, Miller demonstrated a good fit to flight data with this linear model while performing aggressive flight maneuvers. The control input for the analysis was limited to 10% of the vehicle's control input; therefore the results presented here are reasonable values. Although this method has limitation, it can still provide valuable insight on the vehicle's weaknesses when facing disturbances.

5.2 Recommendations for Future Work

The missing piece of this approach is the lack of flight test data to verify the findings of these methods. This is attributable to unforeseen development issues with the microquad, which were elaborated on by Miller [15]. The remaining piece to the successful completion of the microquad lies in a custom built speed control. It has been determined that the COTS ESC from Walkera^{TM} lacks the response and RPM precision that is required for successful autonomous flight. The biggest issue is the current speed controller's repeatability of RPM as well as the fluctuations encountered. These nonlinear characteristics greatly hinder the ability to implement an LTI static controller. Once this problem is eradicated, it is believed that a model based controller can be implemented, and the results presented in this paper can be examined.

A further benefit of improving the ESCs is increase in actuator bandwidth. This could ultimately allow the motors to respond faster. Another way to increase bandwidth is improving the rotor design. By using carbon fiber, the mass of the rotors would decrease, resulting in a lower centripetal force to overcome when changing RPMs. This would require less energy and allow for a faster response, which increases bandwidth. Furthermore, the carbon fiber blades will result in a more efficient rotor. At this scale, rotors become more efficient with decreased thickness. Due to limited options of counter rotating rotors at this scale, the microquad is limited to the GWS^{TM} rotors, which are low quality plastic and extremely out of balance. Carbon fiber rotors can increase motor response and overall efficiency.

Generally, the disturbance derivatives should be the negative of the stability derivatives. For reasons explained in § 3.2, these derivatives did not match with one another. As discussed earlier, Miller had a large range of results for the stability derivatives over 10 different flight tests. It may be beneficial to revisit the identification process and use the results from the bench-top test presented in § 3.3.1. The bench-top test proved to be repeatable and demonstrate strong trends. The identified stability derivatives from the bench-top testing could be used as constants and perform the linear regression again to determine the remaining stability derivatives. If this this adequately fits the flight data, these findings would reinforce the results from the bench-top test, providing increased confidence for the model.

The prediction of the reachability and disturbance ellipsoids needs to go through the mathematical rigors to prove absolutely that a disturbance ellipsoid bounded by the reachability ellipsoid does guarantee disturbance rejection. It is also envisioned that the controllability ellipsoids can be defined through flight test. This is accomplished by having the microquad in hover condition and providing an 'impulse' control input to the vehicle. Using the measurements of the states, one may be able to define the reachability ellipsoid for the microquad. The advantage of this method is that it can capture nonlinear attributes in the system.

A constant disturbance does not accurately represent the atmospheric disturbance a vehicle encounters. A dynamics disturbance is typically represented by driving a shaping filter by a white noise input. This better represents the frequency density of atmospheric disturbances. This has been explored briefly and has shown promising results worth exploring more thoroughly. Another layer to be added is the addition of actuator dynamics to the model. This has also been briefly explored with promising results.

Finally, these analyses are intended to compare the disturbance properties of multiple platforms at this scale. The MAST CTA is exploring several platforms. This type of method will provide good measuring tools when comparing each vehicle. Disturbance rejection is a small piece to the puzzle, but an important element to a vehicle's success operating in urban environments.

Bibliography

[1] S. Zarovy, M. Costello, *Experimental Study of Gust Effects on micro Air Vehicles.* AIAA-2010-7818, AIAA Atmospheric Flight Mechanics Conference. Toronto, Ontario, Canada, August, 2010.

[2] B. Patrick, *Optic Flow Based Station-Keeping and Wind Rejection For Small Flying Vehicles.* Master's Thesis, University of Maryland, College Park, 2010.

[3] W. Pisano, D. Lawrence *Control Limitations of Small Unmanned Aerial Vehicles in Turbulent Environments.* AIAA Guidance, Navigation, and Control Conference. Chicago, Illinois, August, 2009.

[4] S. Boubdallah, *Design and Control of Quadrotors with Application to Autonomous Flying.* Ph.D. Dissertation Ecole Polytech Federale de Laussane, Laussane, Switzerland, 2007.

[5] G. Gremillion, J.S. Humbert, *System Identification of a Quadrotor Micro Air Vehicle.* AIAA-2010-7644, AIAA Atmospheric Flight Mechanics Conference. Toronto, Ontario, Canada, August, 2010.

[6] J.S. Humbert, I. Faruque, *Analysis of Insect-Inspired Wingstroke Kinematic Perturbations for Longitudeinal Control.* Journal of Guidance, Control, and Dynamics. Vol. 34, No. 2, March-April 2011

[7] G. Dullerud, F. Paganini *A Course in Robust Control Theory.* Springer-Veriag, New York, Inc.

[8] J.G. Leishman, *Principles of Helicopter Aerodynamics.* Cambridge University Pres, New York, Second Edition, 2006.

[9] R. Celi, *ENAE635 – Helicopter Stability and Control, Class Notes.* University of Maryland, College Park, 2011.

[10] B.L. Stevens, F.L. Lewis, *Aircraft Control and Simulation.* John Wiley and Sons, Inc., Hoboken, New Jersey, Second Edition, 2003.

[11] Chi-Tsong Chen, *Linear System Theory and Design.* Oxford University Press, Inc., New York, 3nd Edition, 1999.

[12] R.C. Nelson, *Flight Stability and Automatic Control.* McGraw-Hill, New York, 2nd Edition, 1998.

[13] K. Ogata, *Modern Control Engineering.* Pearson Education Inc., New Jersey, 5th Edition, 2010.

[14] C. Harland, J.D. Jacob *Gust Load Testing in a Low-Cost MAV Gust and Shear Tunnel.* AIAA-2010-4539, AIAA Aerodynamics Measurement Technology and Ground Testing Conference. Chicago, IL, July, 2010.

[15] D. Miller, *Open Loop System Identification of a Micro Quadrotor Helicopter from Closed Loop Data.* Master's Thesis, University of Maryland, College Park, 2011.

[16] V. Klein, E.A. Morelli, *Aircraft System Identification: Theory and Practice.* AIAA Education Series, Reston, Virginia, 2006.

[17] J.K. Conroy, J.S. Humbert, D.J. Pines, *System Identification of a Rotary Wing Micro Air Vehicle.* Journal of the American Helicopter Society, Vol. 56, 2011.

[18] J. Gadewadikar, B.M. Chen, *Structured $\mathcal{H}_\infty$ Command and Control-Loop Design for Unmanned Helicopters.* Journal of Guidance, Control, and Dynamics, Vol. 34, No. 4, 2008.

[19] J. Gadewadikar, *H-Infinity Output-Feedback Control: Application to Unmanned Aerial Vehicle.* PhD Thesis, University of Texas at Arlington, 2007.

[20] S. Skogestad, I. Postlethwaite, *Multivariable Feedback Control: Analysis and Design.* John Wiley and Sons, Ltd., Chinchester, West Sussex, UK, 2005.

[21] W.S. Levine, M. Athans, *On the Determination of the Optimal Constant Output Feedback Gains for Linear Multivariable Systems.* IEEE Transactions on Automatic Control, Vol. AC-15, No. 1, 1970.

[22] M. Morari *Design of Resilient Procession Plants - III.* Chemicial Engineering Science Vol. 38. No 11, pp. 1881-1891. 1983.

[23] S. Skogestad, E. Wolff *Controllability Measures for Disturbance Rejection.* IFAC Workshop on interactions between process design and process control, Imperial College, London, Sept. 6-8, 1992.

[24] S. Skogestad, M. Morari *Effect of Disturbance Directions on Closed-Loop Performance.* American Chemical Society, Ind. Eng. Chem. Res 1987, 26, 2029-2035.

[25] O. Kang, Y. Park, M. Suh *New Measure Representing Degree of Controllability for Disturbance Rejection.* Journal of Guidance, Control, and Dynamics. Vol. 32, No. 5, September-October 2009.

[26] F. Hoblit, *Gusts loads on aircraft: concepts and applications.* American Institute of Aeronautics and Astronautics, Inc, 370 L'Enfant Promenade, S.W., Washington, D.C. 20024.